

Excitation of nuclear giant resonances in neutrino scattering off nuclei

Antonio Botrugno and Giampaolo Co'

Dipartimento di Fisica, Università di Lecce
and
Istituto Nazionale di Fisica Nucleare sez. di Lecce,
I-73100 Lecce, Italy

Abstract

The cross sections for neutrino scattering off the ^{12}C and ^{16}O nuclei are calculated within the framework of the continuum Random Phase Approximation. A model to consider also the final state interactions is developed. Total charge-conserving and charge-exchange cross sections for both electron neutrinos and antineutrinos have been calculated up to projectile energies of 100 MeV. The sensitivity of the cross sections to the residual interaction and to the final state interactions is investigated. A direct comparison between neutrino and electron scattering cross sections calculated under the same kinematic conditions is presented. We found remarkable differences between electromagnetic and weak nuclear responses. The model is applied to describe cross sections of neutrinos produced by muon decay at rest and in supernovae explosions.

PACS: 21.60.Jz; 24.30.Cz; 25.30.Pt

1 Introduction

There are various reasons to study the interactions of neutrinos with complex nuclei. A first set of motivations is related to the use of the nucleus as a detector to investigate the neutrino properties [1], for example, the parameters of the flavor oscillations. A second group of motivations is related to use of the neutrinos as a probe in astrophysics [2], and, eventually, in geophysics [3]. Here the importance of the interaction with nuclei is not limited to the detection of the neutrinos, but it is also related to the study of the processes generating them, and to their scattering inside matter (stars, supernovae or earth). Another set of motivations is related to the use of neutrinos to probe the structure of the nucleons and of the nuclei. There is great interest for the possibility of studying the strangeness content of the nucleon with neutrino scattering [4, 5, 6]. Furthermore, neutrinos excite nuclear modes not accessible to the electromagnetic probes, and this allows the study of the characteristics of the nuclear dynamics, and of the nuclear interaction, usually hidden in other processes.

The phenomena above mentioned, involve neutrinos energies varying from a few MeV up to thousand of TeV. In this paper we study processes with neutrinos energies limited to a few tens of MeV. In this case the nucleon degrees of freedom are not excited and we shall be concerned only about the excitation of the nucleus.

Neutrinos with few tens of MeV can excite the nucleus above the nucleon emission threshold, in the region of the giant resonances. The Continuum Random Phase Approximation (CRPA) is the theory most often used to describe the excitation of the nuclear giant resonances. The calculations discussed here have been done by solving the CRPA equations with the Fourier-Bessel technique of Ref. [7]. The CRPA is able to describe, and predict, the position of the various resonances. In the comparison with the experimental data the CRPA cross sections are too large and their widths too narrow. There are good indications that these problems can be solved by extending the RPA configuration space which considers only elementary excitations of one-particle one-hole (1p-1h) type [8, 9]. We call Final State Interactions (FSI) the effects beyond CRPA, to allow for further re-interaction of the emitted nucleon with the remaining nucleus. We have improved the CRPA

description of the total photo-absorption cross sections [10] by developing a phenomenological model that considers the FSI. In this article we present the results obtained by applying the CRPA plus the FSI model to the calculations of neutrino-nucleus cross sections. The primary aim of this work is the study of the consequences of the uncertainties of the nuclear structure model on the description of the neutrinos cross sections.

Even though the formalism we have developed is quite general, we have limited our investigation to the study of the interaction of electron neutrinos, and antineutrinos, with the ^{12}C and ^{16}O nuclei. The two nuclei we have selected are doubly magic nuclei where the CRPA theory is more successful. Furthermore, they are the most important nuclei in liquid scintillators (^{12}C) or water (^{16}O) detectors.

In Sect. 2.1 we discuss in some detail the choice of the CRPA input parameters. The model developed to treat the FSI is presented in Sect. 2.2. Our results are presented in Sect. 3. We first discuss some general features of the neutrino-nucleus cross sections, then we compare electron and neutrino cross sections calculated with the same kinematics. The total cross sections on the ^{12}C and ^{16}O nuclei are shown in Sect. 3.3. In Sect. 3.4 we present the results obtained by applying our model to the case of neutrinos produced by muon decay at rest, and in supernova explosion.

2 The model

In this work we consider the inelastic neutrino-nucleus scattering processes involving both charged current (CC) and neutral current (NC) reactions. The neutrino-nucleus cross section is obtained in plane wave Born approximation and for point-like interaction [11]. In the case of charged leptons we consider the Coulomb distortion by using a Fermi function [12, 13]. The expression of the cross section has been obtained by using the standard trace techniques. We made a non relativistic reduction of the weak current operators, and a multipole expansion of the transition amplitudes [11]. For the nucleon axial form factor we used a dipole expression with axial mass $M_A = 1014$ MeV [14].

This derivation of the cross section is a rather standard one [11], and we do not present it here. A detailed description can be found in Ref. [15]. It may be worth, however, to discuss the final expression of the neutrino-nucleus inclusive cross section, by pointing out the differences with the electron scattering cross section. Under the approximations above mentioned, the electron scattering cross section can be written as a sum of a longitudinal response, i.e. parallel to the momentum transfer direction, produced by the charge operator, and a transverse response, related to the current operator. Also the neutrino-nucleus cross section can be separated into a longitudinal and transverse responses. The novelties in the neutrino scattering are originated by the presence of an axial-vector term of the weak interaction operators in addition to the vector term which is analogous to that of the electromagnetic four-current. For this reason, in the neutrino scattering case, the transverse response is composed by a purely vector term, an axial-vector one and the interference between them. The longitudinal response is composed by a vector Coulomb-like term and two axial terms which interfere with each other. The presence of a single vector term in the longitudinal response is due to the fact that we used the conserved vector current hypothesis. Always in the longitudinal response, the vector and the axial terms do not interfere since they excite states of different parity. Specifically, the vector current excites natural parity states only, while the axial current only unnatural parity states [11].

2.1 Continuum Random Phase Approximation

The evaluation of the hadronic transition matrix elements, requires the knowledge of the wave functions describing the ground state and the excited states of the nucleus. As already anticipated in the introduction, we work in the framework of the CRPA theory. The secular equations of the theory are solved by using the Fourier-Bessel expansion technique developed in [7] and used in the description of various electron scattering processes [16, 17, 18]. We have extended the basic formalism of Ref. [7] to treat charge-exchange excitations. This extension is straightforward, therefore, we do not present here a detailed description of the theory which can be found elsewhere

[15]. We rather prefer to make a discussion of the input parameters necessary to solve the CRPA equations.

The first input required by the CRPA is the mean field used to generate the configuration space of single particle states. The Fourier-Bessel formalism requires single particle states both in the discrete and in the continuum part of the spectrum. For both cases we use the same Woods-Saxon potential of the form:

$$U(r) = U_C(r) + U_{SO}(r) + U_{Coul}(r) \quad (1)$$

with

$$U_C(r) = \frac{V}{1 + \exp[(r - R)/a]} \quad (2)$$

$$U_{SO}(r) = \left(\frac{\hbar}{m_\pi c} \right)^2 \frac{1}{r} \frac{d}{dr} \left(\frac{V_s}{1 + \exp[(r - R_s)/a_s]} \right) \mathbf{l} \cdot \mathbf{s} \quad (3)$$

where m_π is the pion mass, and U_{Coul} is the Coulomb potential, active only for protons, generated by a uniformly charged sphere of radius R_c of total charge $Z - 1$.

The parameters used for the ^{12}C and ^{16}O nuclei are shown in Table 1. They have been chosen to reproduce at best the single particle energies around the Fermi surface and empirical charge density distributions [19]. The ^{12}C parameterization is different from that of Ref. [16], more commonly used in the literature. With this new set of parameters the ^{12}C empirical charge distribution is much better reproduced.

The single particle energies are a crucial ingredient for the solution of the CRPA equations. In the spirit of the Landau-Migdal theory of the finite Fermi systems [20], we used, when available, the experimental single particle energies [21]. In Table 2 we show the single particle states forming the discrete basis of our configuration space, together with the theoretical and experimental energies. In this table, the proton $1d5/2$ and the neutron $1d3/2$ states are included in ^{12}C . In our calculations, these states are in the continuum but the widths of their resonances are so narrow that, for computational reasons, it is more convenient to consider them as bound states with positive energy. The full space used in our calculations is obtained by adding all the continuum states allowing the angular momentum couplings with the hole states up to total angular momentum $J=16$.

The other ingredient required by the CRPA calculations is the residual interaction. We studied the sensitivity of our results to the choice of the residual particle-hole ($p-h$) interaction by making CRPA calculations with three different forces. Their general expression, in momentum space, is:

$$\begin{aligned} V^{ph}(k, \rho) = & \mathcal{K} [F(k, \rho) + F'(k, \rho) \boldsymbol{\tau}(1) \cdot \boldsymbol{\tau}(2) \\ & + G(k) \boldsymbol{\sigma}(1) \cdot \boldsymbol{\sigma}(2) + G'(k) \boldsymbol{\sigma}(1) \cdot \boldsymbol{\sigma}(2) \boldsymbol{\tau}(1) \cdot \boldsymbol{\tau}(2)] \end{aligned} \quad (4)$$

where k is the relative momentum of the $p-h$ pair, and \mathcal{K} a normalization constant. The first two terms have a linear dependence from the nuclear density ρ [22]:

$$F(k, \rho) = F^{ext}(k, \rho) + [F^{int}(k, \rho) - F^{ext}(k, \rho)] \frac{\rho(r)}{\rho(0)} \quad (5)$$

In our calculations we used

$$\rho(r) = \frac{1}{1 + \exp[(r - R)/a]} \quad (6)$$

with $a = 0.5$ and 0.6 fm and $R = 3.0$ and 2.71 fm for ^{12}C and ^{16}O , respectively.

In our calculations we used two interactions of contact type, or zero-range interactions. This means that the functions F , F' , G , and G' of Eqs. (4) and (5) are constant in k . The values of these constants are given in Table 3, and they are labeled LM1 and LM2. The parameters of the LM1 force have been fixed in [22] to reproduce the muonic-atom nuclear polarization energy shifts in the region of the ^{208}Pb nucleus. This parameterization of the interaction has been used in the literature to describe electromagnetic excitations of doubly magic nuclei [7, 16, 17]. The parameters of the second zero-range interaction, LM2, have been fixed in [23] to describe the nuclear spin responses of ^{12}C .

In addition to these two forces we used the polarization potential (PP) of Ref. [24]. This is an effective finite-range interaction containing, in an average way, the contribution of the exchange diagrams. The parameters of this force have been fixed to reproduce some static properties of nuclear matter. The validity of this parameterization has been tested against the results of microscopic calculations of nuclear matter density responses [25]. The PP interaction has been used in the description of the electron scattering quasi-elastic responses [18, 26]. The values of the Landau parameters, obtained in the limit $k \rightarrow 0$, are given in Table 3. The behavior of the various terms of the force as a function of the relative momentum of the $p - h$ pair k is given in Fig. 1.

The values of F , F' , G , and G' presented in Table 3 and in Fig. 1, have been fixed in specific contexts. Since we want to use these interactions in a different context, with a very pragmatical approach, in the spirit of the effective theories, we renormalize each interaction by multiplying it with a constant \mathcal{K} , whose values are given in Table 3. In the case of ^{16}O the values of the constant have been fixed to reproduce the energy of the collective low-lying 3^- state at 6.13 MeV. For the ^{12}C nucleus the constants have been fixed to reproduce the position of the main peak of the total photo absorption cross section at 22.5 MeV. Only the LM2 force in ^{12}C has not been renormalized, since in [23] it was specifically tuned to treat this nucleus, even though the RPA calculations were performed in a discrete single particle basis.

The performances of our CRPA calculations have been tested by comparing the total photo-absorption cross sections with the data measured in Mainz [10]. This comparison is shown in the panels (a) and (c) of Fig. 2. In our CRPA calculations the multipole excitations up to 3^- have been considered, even though the 1^- excitation contributes for more than the 97% of the cross sections shown in the figure.

In ^{16}O the LM1 and PP cross sections almost overlap, while the LM2 is slightly more attractive. In any case the position of the peak is quite well reproduced. As already mentioned, in the ^{12}C case, the good description of the main peak position provided by the LM1 and PP cross sections has been obtained by changing the normalization constant \mathcal{K} . The differences between the two forces becomes evident when observing the other structures of the cross sections. The sharp peak at 17.8 MeV due to the neutron ($1p_{3/2}^{-1}$, $2s_{1/2}$) transition is more strongly excited by the LM1 force. The large peak above 30 MeV, produced by the opening of the $1s_{1/2}$ emission channel, appears at lower energy for the PP force. The LM2 force is more attractive than the other two, also in the ^{12}C case.

The interactions we have adopted, especially LM1 and PP, have been tuned to describe natural parity excitations. These are the most relevant excitations induced by electromagnetic probes. On the other hand, neutrinos are not so selective, and excite indifferently natural and unnatural parity states. This point will be discussed with more details in Sect. 3.2.

We have investigated the reliability of our approach in the description of the unnatural parity excitations. As example of the results of our tests, we show in Table 4 the excitation energies of the 1^+ excitations in ^{12}C charge-conserving and charge-exchange transitions. The agreement with the experimental energies [21] is not very satisfactory, even though the general behavior is respected. It is remarkable that the three forces produce very similar results for the charge-exchange transitions, contrary to what happens in the charge-conserving ones. It is well known in the literature that the description of the unnatural parity excitations improves when tensor terms are included in the $p - h$ interaction [27].

2.2 The FSI model

The limits of the CRPA theory in describing the excitation of the nuclear giant resonances, are evident in Fig. 2. While the positions of the resonances are rather well reproduced, the cross sections are overestimated, and their widths underestimated. The use in the calculations of different interactions does not substantially modify the behavior of the CRPA results. This indicates that the above mentioned problems are not solvable by changing the input of the calculations, but they are related to some of the intrinsic approximations connected to the RPA theory. In the panels

(b) and (d) of Fig. 2, we show the behavior of the sum rule integral

$$SR(\omega) = \int_0^\omega dE \sigma(E) \quad (7)$$

as a function of ω . The various curves in the panels (b) and (d) of the figure have been normalized to the classical value of the Thomas-Reiche-Kuhn (TRK) sum rule: $60NZ/A$ mb. The sum rule integrals of the experimental cross sections are shown by the gray bands.

While all the CRPA results in ^{16}O are below the TRK value, the ^{12}C asymptotic values are above this limit. The presence of the F' and G' functions in our $p-h$ interactions violate the hamiltonian isospin independence hypothesis used to obtain the TRK sum rule values. The effects of these terms of the interaction are larger in ^{12}C than in ^{16}O . A more detailed investigation of this point is beyond the scope of the present article. The information we want to give in this context is that all the CRPA calculations give asymptotic values of the sum rules smaller than those obtained by integrating the experimental cross sections. There is a certain agreement between CRPA results and empirical values up to about 40 MeV in ^{12}C and 30 MeV in ^{16}O but for larger energies, the experimental sum rules are much larger than both the TRK values, and the CRPA curves. There are effects beyond those described by the CRPA, probably short-range correlations effects [28].

As we have already stated in the introduction, the main limitation of the CRPA theory seems to be the restriction of a configuration space where only 1p-1h excitation pairs are considered. The extension of this configuration space, to include more complicated excitations, for example 2p-2h pairs, seems to improve the agreement with the data [8, 9]. In order to take into account effects beyond the RPA we extend a phenomenological model which has been used to describe hadronic processes [23, 29] and electron scattering cross sections in the quasi-elastic region [18, 26, 30]. The model assumes that excitations beyond those considered by the RPA, act as intermediate doorway states. Asymptotically, the nuclear excited states have one particle, in the continuum, and one hole in the residual nucleus. A further assumption consists in considering that, at sufficiently high excitation energies, the contribution of the high-order excitations is independent of the angular momentum of the nuclear excited state. In the quasi-elastic region, the density of states is so high that a specific nuclear excitation characterized by its angular momentum and parity is not relevant any more.

Starting from these hypotheses, it is shown in Refs. [18, 29], that the effects of these high-order excitations, that we shall call henceforth FSI, can be accounted for by a folding integral

$$S^{FSI}(q, \omega) = \int_0^\infty dE S^0(q, E) [h(E, \omega) + h(E, -\omega)] \quad (8)$$

where the folding function is:

$$h(E, \omega) = \frac{1}{2\pi} \frac{\Gamma(\omega)}{[E - \omega - \Delta(\omega)]^2 + [\Gamma(\omega)/2]^2} \quad (9)$$

In the above equations S^0 indicates a known nuclear response for an excitation energy E and a momentum transfer \mathbf{q} . In our case S^0 has been calculated within the CRPA theory.

Fundamental ingredients of the folding model are the functions $\Delta(\omega)$ and $\Gamma(\omega)$ which are linked by a dispersion relation:

$$\Delta(\omega) = \frac{1}{2\pi} P \int_{-\infty}^{+\infty} d\omega' \frac{\Gamma(\omega')}{\omega' - \omega}, \quad (10)$$

where we have indicated with P the principal value integral. The problem is then limited to the determination of the $\Gamma(\omega)$ function. In a microscopic approach, this function has to be evaluated by calculating all the many-particle many-hole transitions induced by the residual interaction. In practice, we extract $\Gamma(\omega)$ from an empirical description of the imaginary part of the single particle self-energy. The data we have considered for positive values of ω are those related to the imaginary part of the optical potential whose parameters have been fixed to fit nucleon-nucleus elastic scattering cross sections. For negative values of ω we have considered the energy width of

the single particle levels, measured in knock-out reactions like $(e, e'p)$ or (p, d) . We have obtained $\Gamma(\omega)$ by making the average of the single particle energy width $\gamma(\omega)$:

$$\Gamma(\omega) = \frac{1}{\omega} \int_0^\omega d\varepsilon [\gamma(\varepsilon + \omega) + \gamma(\varepsilon - \omega)] . \quad (11)$$

The empirical values of the single particle widths [31] have been fitted by using the following expression of γ :

$$\gamma(\varepsilon) = A \left(\frac{\varepsilon^2}{\varepsilon^2 + B^2} \right) \left(\frac{C^2}{\varepsilon^2 + C^2} \right) \quad (12)$$

Another correction to our CRPA calculations is related to the non-locality of the mean field. A simple way to take into account this important correction is the introduction of an effective mass of the nucleon m^* [31]. For a given value of m^*/m the following scaling relation holds:

$$S_{m^*}(q, \omega) = \frac{m^*}{m} S_m \left(q, \frac{m^*}{m} \omega \right) . \quad (13)$$

Our FSI model conserves the sum rules. No further strength is added to that provided by the RPA. The effect of the FSI is a redistribution of the strength.

The parameterization of the γ function and of m^* given in the lowest row of Table 5 allows us to reproduce the electromagnetic quasi-elastic responses in various nuclei [18, 26, 30, 32]. In the giant resonance region some of the assumptions used to derive the model are not longer valid, for example, the independence of the γ function from the angular momentum and the parity of nuclear excitation. We forced our model to work also in the giant resonance region by considering an energy dependence of the A , B and m^* parameters. For energies greater than 40 MeV, the values of these parameters are those used in the quasi-elastic region. We fix the A , B and m^* values at 10 MeV, and we let them evolve linearly up to 40 MeV, where they reach their asymptotic values. The values at $\varepsilon = 10$ MeV have been fixed to reproduce at best, within this model, the photo-absorption data of Mainz [10]. The full set of parameters is given in Table 5.

We show in Fig. 3 the effects of the model. In all the panels of the figure the thin full lines represent the CRPA results. The application of our FSI model by using the quasi-elastic parameters, lowest row of Table 5, produces the dashed lines. The thick full lines show the results obtained with the energy dependent parameterization. The effect of the FSI is evident, the peaks of the cross sections are lowered, and their widths become larger. The asymptotic parameterization has too strong an effect on the CRPA cross sections. In order to simplify the discussion, we have used a unique parameterization for all the interactions and for both nuclei, for this reason the agreement with the data is not of the same quality for all the cases considered.

We have tested the validity of our model against the available electron scattering data. We have not been able to find inclusive electron scattering data in the giant resonance region for the ^{16}O nucleus. The agreement with the available ^{16}O quasi-elastic data [33] is quite satisfactory as has been shown in Ref. [32].

The test comparison in Fig. 4 is done with ^{12}C data only. For the sake of brevity, we show only the results obtained with the LM1 interaction. The other interactions produce very similar curves. The data shown in the (d),(e),(f) panels of the figure are lowest energy cross sections measured in Saclay [34] in the framework of an experimental program aimed to separate charge and current quasi-elastic responses by means of a Rosenbluth technique. For this reason few points have been measured in the giant resonance region. To the best of our knowledge, the data shown in the (a), (b) and (c) panels have never been published. We have taken them from Ref. [35] where they are quoted. These data cover part of the giant resonance region.

The results of Fig. 4 show that the application of the FSI model improves considerably the agreement with the data. This was somehow expected, since the set of multipoles dominating the photo-absorption cross section and the electron scattering cross section are quite similar. Our FSI model describes rather well the inclusive ^{12}C electron scattering data in the quasi-elastic region [18, 26, 30].

3 Results

The model described in the previous section has been applied to the description of neutrino scattering off the ^{12}C and ^{16}O nuclei. We first discuss some characteristics of the neutrino cross sections independent of the nuclear structure details. Then, we make a comparison between electron and neutrino cross sections under the same kinematic conditions. The discussion of these two points is necessary for a better understanding of the following section where we discuss the interplay between the nuclear structure model and the neutrino induced nuclear excitations. Finally, we apply our model to two specific cases: the neutrino emission from muon decay at rest, and from supernova explosion.

3.1 Some general features of the neutrino-nucleus cross sections

All the results presented in this section have been obtained with CRPA calculations by using the LM1 interaction and without the application of the FSI model.

In Fig. 5 we show the squares of the hadronic transition matrix elements as a function of the nuclear excitation energy. We have considered three neutrino scattering processes, and two neutrino incoming energies. The transition amplitudes have been calculated for the scattering angle $\theta = 30^\circ$. The tree left panels show the results for a nuclear excitation in the giant resonance region, with momentum transfer values varying between 27 and 42 MeV/c. The results shown in the right panels are related to the excitation of the quasi-elastic peak with momentum transfer values varying between 512 and 526 MeV/c.

In all the panels the full lines show the contribution of the transverse axial vector operators, while the dashed lines show the contribution of the transverse vector operators. The other lines are related to the longitudinal terms of the cross section. Specifically, the dotted lines show the axial longitudinal contributions, the dotted-dashed those of the axial Coulomb-like, and the dotted-dashed lines those of the vector Coulomb-like terms.

The cross section is obtained by adding to the terms shown in Fig. 5 the interference terms, and by multiplying all of them with the leptonic terms. This changes only slightly the relative weight of the various terms. In all the cases we have investigated, the transverse axial vector currents dominate the cross sections [15].

The other very general trend, is that of the axial Coulomb term whose contribution to the cross sections is always orders of magnitudes smaller than those of the other currents. These results are in agreement with those of Ref. [36]. The behavior of the other current operators is more complicated. Their role changes depending upon the reaction and the kinematics. For example, the charge-exchange reactions in the quasi-elastic region show remarkable contributions of the transverse vector operator, usually smaller than the contributions of the longitudinal axial operators.

Another point we want to discuss is the angular distribution of the emitted lepton. In Fig. 6 we show the results of calculations done for fixed nuclear excitation energy, 20 MeV, and for different values of the projectile energy ε_i . The double differential cross sections have been integrated on the angle. These are what we call σ_{tot} in the figure, and their behavior as a function of ε_i is shown in the panel *e*. The ratios between the double differential cross sections and σ_{tot} are shown in the panels (*a* – *d*) as a function of the scattering angle θ . In these panels the various lines show the results obtained with the values of ε_i given in the lower right part of the figure. In agreement with the results of Refs. [37] and [38] we found a common trend of all the reactions considered: with increasing ε_i the angular distributions become forward peaked. For the lowest values of ε_i we have used, 50 and 100 MeV, the cross sections are larger in the backward than in the forward direction. This behavior is more pronounced in the charge-exchange reactions, (*b*) and (*d*) panels. In any case, the relative differences between the cross section values in the angular distributions is smaller at lower energies than at high energies. The absolute values of the cross sections can be estimated from the results shown in the (*e*) panel. The values of σ_{tot} increase about two order of magnitude when ε_i varies from 50 up to 200 MeV. After that, the increase of the cross section is much slower. The results we have shown are relative to a specific value of the excitation energy, but we found the same behavior for all the energies investigated [15].

3.2 Electron versus neutrino scattering

There are many analogies between electron and neutrino scattering processes. For this reason electron scattering data can be used to make predictions about neutrino cross sections [39, 40]. In Figs. 7 and 8 we compare the nuclear excitations induced by both probes, in the same kinematic conditions. All the results have been obtained by using the CRPA and considering multipole excitations up to $J=12$. In Fig. 7 the energy of the incoming lepton has been fixed at 50 MeV, and two values of the scattering angle have been used: $\theta = 30^\circ$ and 150° . In Fig. 8 we considered a lepton incoming energy of 1 GeV and $\theta = 30^\circ$.

Let's first discuss Fig. 7 where the nuclear giant resonances are in general excited. The behavior of the electron scattering cross sections is well known. The cross section at forward scattering angles is ruled by the longitudinal response, which is excited only by natural parity multipoles. At backward angles the transverse response, excited by both natural and unnatural parity multipoles, dominates. Furthermore, the values of the cross sections decrease with increasing incoming energy and scattering angle. All these characteristics are present in our results. It is worth pointing out the change of scale in the panels (a) and (c). To facilitate the discussion we show in Table 6 the percentage contribution of the various multipoles to the energy integrated cross sections of Fig. 7. The electron scattering cross section is dominated by the 1^- excitation for $\theta=30^\circ$, as is shown in Table 6. The same table shows that, with increasing scattering angle, the role of the 1^- excitation decreases, while that of the 2^+ and of the 2^- increases. This is a sign of the relevance of the transverse response. The broad peaks at 23.2 MeV are due to the 1^- , multipole responsible also of the sharp peak at 19.7 MeV. The sharp excitation at 20.1 MeV, which is enhanced at $\theta=150^\circ$, is due to the 2^- multipole.

The situation is quite different for the neutrino scattering cross sections. The shapes of all the neutrino cross sections have little resemblance with those of electron scattering cross section. A difference with the charge-exchange reactions was expected, since the basic particle-hole transitions are not those excited in electron scattering. The difference with the charge-conserving cross section is more surprising. It is shown in Table 6 that the neutrino cross sections are not dominated by the 1^- multipole, even at small scattering angles. In effect, the contribution of the 2^- multipole is relevant in all the cross sections. This multipole is responsible for the peak at 20.1 MeV in the (ν, ν') cross section. We have also verified that the $(\bar{\nu}, \bar{\nu}')$ cross section, which is not shown in the figure, has a sharp peak in the same position, corresponding to the analogous excitation in (e, e') . It is interesting to notice that in the experimental electromagnetic spectrum, there is a 2^- state at 20.43 MeV [21]. Our (ν, e^-) cross section shows a 2^- sharp peak at 23.40 MeV to be compared with a 2^- state at 24.09 MeV found in (p, n) reactions [41].

The features we have just discussed are understood by observing that, in all the neutrino processes we have studied, the axial vector part of the weak current dominates on all the other cross section terms. To be more specific, as shown in Fig. 5, the transverse axial terms, are usually orders of magnitude larger than the other terms of the cross section. For this reason, in neutrino scattering there is no dominance of the natural parity multipoles, contrary to what happens with the electromagnetic interaction.

The dominance of the axial current has consequences also in the quasi-elastic excitation, as we show in Fig. 8. The shapes of the various cross sections are rather similar, and they show the quasi-elastic peak at the same value of the excitation energy $\omega = 150$ MeV. The differences become evident when the contribution of each multipole to the total cross section is explicitly studied. In the figure the progressive sum of these contributions, which finally gives the full line, is presented by the thin dashed lines. The contributions are ordered with increasing value of the angular momentum, and for each multipole, we show first the negative parity contribution, and then, that of the positive parity. The staggering shown in the electron scattering results, is due to the fact that natural parity multipoles contribute more than the unnatural parity ones, because the relatively small value of the scattering angle favors the longitudinal response. In neutrino scattering, the contribution of the various multipoles is more regularly distributed, without any particular difference between natural and unnatural parity states. From the above observations we conclude that the procedure proposed in Ref. [40] to predict neutrino cross sections by using universal response functions extracted from electron scattering data, should be used with caution,

if at all.

An analogous study has been done for the ^{12}C nucleus. For sake of brevity we do not show here the results, which in the case of quasi-elastic region are similar to those of ^{16}O . In the giant resonance region, we observed that in ^{12}C , the role of the 2^- is not as remarkable as in ^{16}O . In ^{12}C the excitation of the 1^+ multipole is more important.

3.3 The sensitivity to the nuclear model

In this Section we discuss the stability of our results against the uncertainties related to the choice of the residual interaction, and the influence of the FSI.

In Fig. 9 we show the differential cross sections for various neutrino scattering processes. The target is the ^{16}O . The projectile energy, ε_i , has been fixed at 50 MeV, and the double differential cross sections have been integrated on the angular distribution of the scattered lepton. The cross sections have been obtained by using the three residual interactions presented in Sect. 2.1. The dispersion of the results of Fig. 9 is larger than that relative to the photo-absorption, see Fig. 2. The positions of the peaks change with the interaction, and also the heights and the widths of the resonances. This sensitivity to the residual interaction is comparable to that shown in Refs. [36] and [42].

In Fig. 9 the cross sections show narrow peaks. In our CRPA calculations the widths of the resonances are due, exclusively, to the proper treatment of the continuum, the so-called escape width. The various processes shows different type of resonances. The $(\bar{\nu}, e^+)$ cross sections shows peaks between 15 and 20 MeV, while the (ν, e^-) cross sections between 22 and 30 MeV. The resonances of the charge-conserving (ν, ν') and $(\bar{\nu}, \bar{\nu}')$ reactions are positioned between 19 and 25 MeV. Also the widths of these peaks are quite different. They are narrower in $(\bar{\nu}, e^+)$ than in the other processes. All these features can be understood by considering that the different processes excite different $p - h$ configurations.

The comparison between the two charge-conserving reactions, panels (a) and (b) of Fig. 9, indicates that, in our calculations, neutrinos and antineutrinos excite the same resonances. For each interaction, our results show a perfect coincidence between the position of the peaks of the neutrino and those of the antineutrinos cross sections. This was an expected result, since the two processes imply the same configuration space. We did not find any trace of the effects presented in Refs. [42] and [43].

In general, the antineutrino cross sections are smaller than the neutrino ones. This effect becomes evident in the total cross sections.

All the cross sections shown in Fig. 9 have been calculated within the CRPA framework. To illustrate the effects of the FSI, we show in the panel (a) of Fig. 10 the transverse axial response. The full line shows the CRPA response obtained with the LM1 interaction. The value of the momentum transfer has been fixed, and the response has been calculated for various values of the nuclear excitation energy. It is important to notice that, in the response, the two kinematic variables q and ω are independent. The application of our FSI model, produces the dashed line. As expected, the CRPA strength is redistributed. The peaks become smaller and broader, and the strength is mainly shifted toward the high energy tail. The strength moved at higher energies is lost when the response is inserted in the cross section, since in this case q and ω are related by kinematics constraints. For example ω cannot be larger than q . This fact provokes a general reduction of the total cross section.

In the panel (b) of Fig. 10 we show the effect of the FSI on the cross section. The full line shows the CRPA result. The naive application of the folding model to the cross section produces the dotted line. This procedure is incorrect, since it involves also the leptonic terms, which are momentum and energy dependent. The correct procedure consists in applying the folding model to the responses. The cross section is then calculated by using the folded responses. In the figure, the dashed line shows the cross section obtained in this last, correct, manner. Also in this case the peaks are lowered and smoothed, but their positions do not change as strongly as in the naive approach. More striking is the fact that the behavior in the higher energy region is rather similar to that of the unfolded cross section.

The total cross sections, obtained by integrating on the scattering angle and on the nuclear excitation energy, are shown in Figs. 11 and 12, for ^{12}C and ^{16}O respectively, as a function of the projectile energy ε_i . Since the cross sections values vary by orders of magnitude, we present them in both linear and logarithmic scales, which emphasize different aspects. The cross sections shown in the figures have been obtained by using the three interactions, and all contain the FSI effects. These are the main results of our work.

In Fig. 13 we present the effects of the FSI by showing the following ratios between total cross sections:

$$T(\varepsilon_i) = \frac{\sigma^{RPA}(\varepsilon_i) - \sigma^{FSI}(\varepsilon_i)}{\sigma^{RPA}(\varepsilon_i) + \sigma^{FSI}(\varepsilon_i)} \quad (14)$$

as a function of the projectile ε_i . for the various total cross sections. The behavior of $T(\varepsilon_i)$ at low values of ε_i , can be understood by considering that, in the evaluation of the total cross sections, only the differential cross sections with excitation energies close to the nucleon emission threshold enter. Part of the strength removed by the FSI from the giant resonance region, goes to lower energies, i.e. in the region we are discussing. Therefore, in general, at low ε_i the FSI cross section is larger than σ^{RPA} . The exceptions to this trend are due to the presence of sharp peaks in the threshold region. These peaks are smoothed by the FSI. At low ε_i values the sensitivity to the residual interaction is remarkable.

This situation changes at higher ε_i values, where the various results stabilize their behaviors around a specific value. For $\varepsilon_i \geq 40$ MeV, the effect of the FSI presented, and discussed, in Fig. 10 starts to be effective, therefore the σ^{FSI} is smaller than σ^{RPA} , and this produces the positive values of $T(\varepsilon_i)$. The asymptotic values of the ratios indicate the reduction factor produced by the FSI. These values vary between 0.05 and 0.10 in agreement with the results of Refs. [32, 44, 45] where the quasi-elastic regions have been investigated.

The effects of the various residual interactions on the total cross sections of Figs. 11 and 12 do not have systematic trends. Each reaction, and nucleus, should be separately analyzed. The logarithmic plots indicate that, at low energy values, the differences in ^{12}C are larger than those found in ^{16}O . It is evident that LM2 results in the $^{12}\text{C} (\bar{\nu}, e^+)^{12}\text{B}$ reactions are remarkably larger than the other ones. This is due to the fact that in the LM2-CRPA calculation a strong 1^+ resonance appears above the nucleon emission threshold. This does not happens for the other two interactions.

We emphasize the differences between the total cross sections calculated with the various interactions, by showing in Fig. 14 the ratios between the total cross sections and the LM1 total cross sections taken as a reference calculation. The meaning of the lines is the same as in Figs. 11 and 12, therefore the LM1 results are represented by horizontal lines with value 1. In ^{12}C the LM2 results are larger than those obtained with the LM1 interaction for all the reactions but for the (ν, e^-) one. In this case, the PP result is noticeably different from the other two. At higher energies there is a convergence of all the results. As we have already pointed out the LM2 results for the $(\bar{\nu}, e^+)$ reaction, remain above the other ones, even in the asymptotic region.

The results for the ^{16}O nucleus show a much better agreement, or in other words, a smaller sensitivity to the residual interactions. As in ^{12}C the main differences between the various calculations are located in the low energy region. All the calculations show convergence at high energies. Only the results of the charge-conserving reactions at 100 MeV do not converge to LM1 values.

3.4 Specific applications

We have used the total cross sections of Figs. 11 and 12 to study two specific situations: the electron neutrinos emitted by the muon decay at rest, and those emitted after a supernova explosion.

The energy distribution of the neutrinos emitted by a muon, follows the law [46]:

$$W(\varepsilon_i) = \mathcal{N} \varepsilon_i^2 \left(\frac{m_\mu^2 - m_e^2}{2m_\mu} - \varepsilon_i \right) \quad (15)$$

where m_μ and m_e are the muon and electron mass respectively, and \mathcal{N} a normalization constant

fixed such that the integral of $W(\varepsilon_i)$ is 1. The normalized function $W(\varepsilon_i)$ is shown in the panel (a) of Fig. 15.

The ^{12}C (ν, e^-) ^{12}N flux averaged cross sections

$$\langle \sigma(\varepsilon_i) \rangle = \sigma(\varepsilon_i) W(\varepsilon_i) \quad (16)$$

are presented in the panel (b) of Fig. 15 as a function of the neutrino energy. All the results obtained with the three residual interactions, with and without the inclusion of the FSI, are shown in the figure. The thinner lines present the CRPA results, while the thicker lines are the results which include the FSI. The results obtained with the same residual interaction are identified by the same line type. The FSI interaction lowers the CRPA results in all the cases. This effect is larger for the PP potential than in the other two cases. At the peak of the distribution the lowering effect is 22% for the PP and 12% for the other two interactions. The effect of the FSI is comparable with the uncertainty related to the choice of the residual interaction.

The maxima of the flux averaged cross sections are around $\varepsilon_i=45$ MeV. For this value of the neutrino energy, we show in the panel (c) of Fig. 15, the behavior of the angular integrated differential cross sections as a function of the nuclear excitation energy. The curves represent the CRPA results, without FSI. The LM1 cross section show a large resonance around 24 MeV, and a narrow peak at 20 MeV. In the PP cross section, this last peak is positioned at lower energy, and it is higher. The LM2 and PP cross sections exhibit their main peaks at the same energy. The LM2 result, shows, in addition, smaller peak at about 25 MeV. These differences are the source of the variations in the flux averaged cross sections of panel (b).

A comparison with experimental data [47, 48, 49] is done in Table 7. In this table we show the values of the total cross sections obtained by integrating the flux averaged cross sections of the panel (b). Our results are lower than the empirical ones. They are also remarkably lower than those obtained by other authors which used ordinary RPA [50], Continuum RPA [51, 52, 53], quasi-particle RPA [54, 55] shell model [56], infinite nuclear matter models in local density approximation [57, 58]. The source of these discrepancies is related to the fact that our cross sections have been calculated only above the continuum threshold. We have neglected the excitation of the discrete spectrum. Some of these discrete excitations are important for the neutrino energies involved in the process, for example the 1^+ state at 17.34 MeV, just below the continuum threshold. This can explain why calculations working with discrete configuration spaces [50, 54, 55, 56] produce cross sections larger than ours.

The other application of our results we want to discuss is related to the inelastic neutrino scattering reactions relevant for the nucleosynthesis following the supernova explosion. Monte Carlo simulations [59, 60] indicate that the energy distribution of the neutrinos produced in a supernova explosion can be rather well described by the function:

$$f(\varepsilon_i) = \mathcal{C} \frac{\varepsilon_i^2}{1 + \exp(\varepsilon_i/T - \alpha)} \quad (17)$$

where \mathcal{C} is a constant fixed to normalize $f(\varepsilon_i)$ to unity. The average energy of the produced electron neutrinos,

$$\langle \varepsilon_i \rangle = \int_0^\infty \varepsilon_i f(\varepsilon_i) d\varepsilon_i \quad (18)$$

can assume values from 11 up to 12 MeV, and the parameter α can vary between 0 and 5 [60].

We have multiplied the (ν, ν') cross sections of Figs. 11 and 12 with the energy distribution (17). We wanted to compare the effects of the nuclear structure uncertainties with those related to $f(\varepsilon_i)$. For this reason our cross sections have been multiplied by the energy distributions (18), obtained with three different parameters sets, whose values are given in Table 8. The respective energy distributions are shown in the panel (c) of Fig. 16.

The flux averaged cross sections for ^{12}C and ^{16}O nuclei are presented in the panels (a) and (b) of Fig. 16 respectively. For each nucleus we show the results obtained by using the three different interactions for the three different parameterizations of $f(\varepsilon)$. The various types of line identify the interactions used, and the roman numbers the various parameterizations of $f(\varepsilon_i)$.

We have verified that the effect of the FSI is negligible. The relevant nuclear structure effects are related to the residual interactions. The uncertainties produced by different choices of the interaction are comparable with those related to the choice of the $f(\varepsilon_i)$ parameters.

We should point out that our cross sections have been calculated only for $\varepsilon_i > 20$ MeV, and for nuclear excitation energies above the continuum threshold. This means that in our results, the most important part of the energy distribution $f(\varepsilon_i)$, which is peaked around 9, 10 MeV, does not contribute. Our results are strongly related to the high energy tails of the $f(\varepsilon_i)$ distributions which we emphasized by using the logarithmic scale in the insert of the panel (c).

4 Conclusions

In this article we have presented the results of calculations for the electron neutrino, and antineutrino, scattering cross sections off ^{12}C and ^{16}O nuclei. The neutrino energy range of our interest goes from a few tens of MeV up to a few hundreds of MeV. The nuclear transitions, of both charge-conserving and charge-exchange type, have been described within the CRPA theory implemented by a model which considers the FSI effects. The parameters of our nuclear model have been fixed to reproduce total photo-absorption cross section data, Fig. 3, and the validity of the model has been tested against electron scattering data, Fig. 4.

In all the kinematics we have studied, the transverse axial vector responses give the largest contributions to the cross sections, Fig.5. We have also investigated the angular distributions of the various cross sections as a function of the projectile energy, Fig. 6. We found that at low energies, $\varepsilon_i = 50$ MeV, all the cross sections are backward peaked. This behavior is smoothly modified, and already at 200 MeV all the cross sections are forward peaked. For energies above 200 MeV this behavior becomes more accentuated, i.e. the ratio between the cross section values at forward and backward directions increases.

We have found large differences between neutrinos and electron scattering cross sections calculated for the same kinematic conditions in the giant resonance region, Fig. 7. The various probes excite resonances which differ in energy, angular momentum and parity. This was expected in the charge-exchange processes, since, in this case, the particle-hole configuration space is different from the electron scattering reaction. We have found remarkable that also the charge-conserving neutrino, and antineutrino, cross sections show different shapes with respect to those of the electron scattering cross sections. We identified the source of these differences with the dominance of the transverse axial vector terms in the neutrino reactions.

Our main results, the total cross sections for both nuclei as a function of the projectile energy, have been presented in Figs. 11 and 12. For neutrino energies above 40 MeV the effect of the FSI is a reduction of the cross sections of about 10-20%, depending upon the nucleus and the reaction considered. For lower neutrino energies the FSI effects do not have a common trend, Fig. 13.

The sensitivity of our results to the residual interaction is weak for neutrino energies above 40 MeV. The various cross sections agree within a 10% of accuracy. In this region, we found agreement also with cross sections calculated by other authors [51, 61, 62, 63]. This gives us confidence about the reliability of the nuclear model.

The situation for neutrino energies below 40 MeV is more complicated. In this case, the cross sections are sensitive only to the excitation region around the nucleon emission threshold and the giant resonances. This excitation energy region, is very difficult to describe, since the CRPA results both depend strongly on the ingredients of the nuclear structure models, i.e. single particle energies and residual interactions. Unfortunately, this problem is not irrelevant for neutrino physics. We have shown that the energy distributions of the neutrinos produced by muon decay at rest, see Fig. 15, and also that of the neutrinos emitted from a supernova remnant, Fig. 16 are most sensitive to the low energy neutrinos. Also in the proposed beta-beam facilities [64], the neutrino energy distributions have their maxima in the region emphasizing the excitation of nuclear giant resonances [65].

From the nuclear structure point of view, the situation is quite intriguing. An improvement of our capability of describing the nuclear excitation in the continuum is necessary. From the experimental point of view, (e,e') data in the giant resonance region for the ^{12}C and ^{16}O nuclei are

required to test the validity of our nuclear structure models. However, being able to describe these data would not be sufficient to be sure about the description of neutrino-induced excitations. We have shown that, even in the neutral-current case, neutrinos calculations are sensitive to nuclear structure details that are irrelevant in electromagnetic excitations. Therefore, it is evident the need of comparisons with hadron excited giant resonance data [23], especially to test charge-exchange results.

Acknowledgments

We thank F.Cavanna and F.Vissani for useful discussions, and A.M.Lallena and P. Rotelli for their interest in the work and for their comments about the manuscript. This work has been partially supported by the MIUR through the PRIN *Fisica del nucleo atomico e dei sistemi a molticorpi*.

References

- [1] J.Morfin, M.Sakuda, Y.Suzuki, eds., Nucl. Phys. B, Proc. Suppl., 112 (2002);
F.Cavanna, C.Keppel, P.Lipari, M.Sakuda, eds., Nucl. Phys. B, Proc. Suppl., 139 (2005).
- [2] F.Cavanna, M.L.Costantini, O.Palamara, F.Vissani, Surveys High Energy Phys. 19 (2004) 35.
- [3] G.Fiorentini, F.Mantovani, B.Ricci, Phys. Lett. B 557 (2003) 139;
F.Mantovani, L.Carmignani, G.Fiorentini, M. Lissia, Phys. Rev. D 69 (2004) 013001.
- [4] G.T.Garvey, S.Krewald, E.Kolbe, K.Langanke, Phys. Lett. B 289 (1992) 249;
G.T.Garvey, E.Kolbe, K.Langanke, S.Krewald, Phys. Rev. C 48 (1993) 1919.
- [5] M.J. Musolf et al., Phys. Rep. 239 (1994) 1.
- [6] W.M.Alberico, S.M.Bilenky, C.Maieron, Phys. Rep. 358 (2002) 227.
- [7] R.de Haro, S.Krewald, J.Speth, Nucl. Phys. A 388 (1982) 265.
- [8] S.Drożdż, S.Nishizaki, J.Speth, J.Wambach, Phys. Rep. 197 (1990) 1.
- [9] S.Kamerdzhev, J.Speth, G.Tertychny, Phys. Rep. 393 (2004) 1.
- [10] J.Ahrens, et al., Nucl. Phys. A 251 (1975) 479.
- [11] J.D.Walecka, Muon Physics vol. 2, V.W.Hughes and C.S.Wu eds., Academic Press, New York, 1975, 113.
- [12] J.M.Blatt, V.F.Weisskopf, Theoretical nuclear physics, John Wiley and Sons, New York, 1952.
- [13] J. Engel, Phys. Rev. C 57 (1998) 2004.
- [14] V.Bernard, L.Elouadrhiri, U.G.Meißner, J. Phys. G 28 (2002) R1.
- [15] A.Botrugno, Ph. D. thesis, Lecce University (2004), unpublished;
<http://www.fisica.unile.it/~gpc/ps/botrugno-phd.ps.gz>
- [16] G.Co', S.Krewald, Phys. Lett. B 137 (1984) 145.
- [17] G.Co', S.Krewald, Nucl. Phys. A 433 (1985) 392.
- [18] G.Co', K.Q.Quader, R.Smith, J.Wambach, Nucl. Phys. A 485 (1988) 61.
- [19] C.W.De Jager, C.De Vries, At. Data and Nucl. Data Tables 36 (1987) 495.
- [20] A.B.Migdal, Theory of finite Fermi systems, Interscience, New York, 1967.

- [21] C.M.Lederer, V.S.Shirley, Table of Isotopes, Wiley and Sons, New York, 1978.
- [22] G.Rinker, J.Speth, Nucl. Phys. A 306 (1978) 360.
- [23] F.T.Baker, et al., Phys. Rep. 289 (1997) 235.
- [24] D.Pines, K.Q.Quader, J.Wambach, Nucl. Phys. A 477 (1988) 365.
- [25] S.Fantoni, V.R.Pandharipande, Nucl. Phys. A 473 (1987) 234.
- [26] J.E.Amaro, G.Co', A.M.Lallena, in Electromagnetic Response Functions of Nuclei, R. Cenni ed., Nova Science (Huntington,NY) 2001.
- [27] J.Speth, V.Klemt, J.Wambach, G.E.Brown, Nucl. Phys. A 343 (1980) 382;
G.Co', A.M.Lallena, Nucl. Phys. A 510 (1990) 139.
- [28] A.Fabrocini, S.Fantoni, Nucl. Phys. A 435 (1985) 448;
E.Lipparini, S.Stringari Phys. Rep. 175 (1989) 103;
G.Orlandini, M.Traini, Rep. Prog. Phys. 54 (1990) 257.
- [29] R.D.Smith, J.Wambach, Phys. Rev. C 38 (1988) 100.
- [30] J.E.Amaro, G.Co', A.M.Lallena, Nucl. Phys. A 578 (1994) 365.
- [31] C. Mahaux, N.Ngô, Nucl. Phys. A 378 (1982) 205.
- [32] G.Co', C.Bleve, I.De Mitri, D. Martello, Nucl. Phys. B, Proc. Suppl., 112 (2002) 210.
- [33] M. Anghinolfi, et al., Nucl. Phys. A 602 (1996) 405.
- [34] P. Barreau et al. Nucl. Phys. A 402 (1983) 515.
- [35] E.Kolbe, K.Langanke, P.Vogel, Nucl. Phys. A 613 (1997) 382.
- [36] N.Jachowicz, S.Rombouts, K.Heyde, J.Ryckebusch, Phys. Rev. C 59 (1999) 3246.
- [37] W.C.Haxton, Phys. Rev. D 36 (1987) 2283.
- [38] E.Kolbe, K.Langanke, G.Martínez-Pinedo, P.Vogel, J. Phys. G 29 (2003) 2569.
- [39] K.Langanke, G.Martínez-Pinedo, P.von Neumann-Cosel, A.Richter, Phys. Rev. Lett. 93 (2004) 202501.
- [40] J.E.Amaro et al. Phys. Rev. C 71 (2005) 015501.
- [41] A.Fazely, et al. Phys. Rev. C 25 (1982) 1760.
- [42] E.Kolbe, K.Langanke, S.Krewald, F.K.Thielemann, Nucl. Phys. A 540 (1992) 599.
- [43] E.Kolbe, K.Langanke, S.Krewald, Phys. Rev. C 45 (1992) 2464.
- [44] C.Bleve et al., Astroparticle Phys. 16 (2001) 145.
- [45] A.Botrugno, G.Co', Eur. Phys. Jour. A 24 s1 (2005) 109.
- [46] L.Michel, Proc. Phys. Soc. (London) A 63 (1950) 514;
H. Überall, Nuovo Cimento 23 (1962) 219.
- [47] D.A.Krakauer et al. Phys. Rev. C 45 (1992) 2450.
- [48] C.Athanassopoulos et al. Phys. Rev. C 55 (1997) 2806.
- [49] B.E.Bodmann et al. Phys. Lett. B 332 (1994) 251.
- [50] N.Auerbach, N.Van Giai, O.K.Vorov, Phys. Rev. C 56 (1997) R2368.

- [51] E.Kolbe, K.Langanke, P.Vogel, Nucl. Phys. A 652 (1999) 91.
- [52] E.Kolbe, K.Langanke, S.Krewald, Phys. Rev. C 49 (1994) 1122;
E.Kolbe, Phys. Rev. C 54 (1996) 1741.
- [53] N.Jachowicz, K.Heyde, J.Ryckebusch, S.Rombouts, Phys. Rev. C 65 (2002) 025501.
- [54] C.Volpe et al., Phys. Rev. C 62 (2000) 015501.
- [55] F.Krmpotić, A.Mariano, A.Samana, Phys. Lett. B 541 (2002) 298;
F.Krmpotić, A.Samana, A.Mariano, Phys. Rev. C 71 (2005) 044319.
- [56] A.C.Hayes, L.S.Towner, Phys. Rev. C 61 (2000) 044603.
- [57] S.K.Singh, E.Oset, Phys. Rev. C 48 (1993) 1246;
T.S.Kosmas, E.Oset, Phys. Rev. C 53 (1996) 1409;
S.K.Singh, N.C.Mukhopadhyay, E.Oset, Phys. Rev. C 57 (1998) 2687.
- [58] J.Nieves, E.Amaro, M.Valverde, Phys. Rev. C 70 (2005) 055503.
- [59] H.T.Janka, W. Hillebrandt, Astronom. Astrophys. 224 (1989) 49.
- [60] M.T.Keil, G.G.Raffelt, H.T. Janka, Astrophys. J. 590 (2003) 971.
- [61] E.Kolbe, K.Langanke, F.K.Thielemann, P.Vogel, Phys. Rev. C 52 (1995) 3437.
- [62] E.Kolbe, K.Langanke, P.Vogel, Phys. Rev. D 66 (2002) 013007.
- [63] T. Kuramoto, M. Fukugita, Y. Kohyama and K. Kubodera, Nucl. Phys. A 512 (1990) 711.
- [64] M.Mezetto, Jour. Phys. G 29 (2003) 1781;
C.Volpe, Jour. Phys. G 30 (2004) L1.
- [65] G.C.McLaughlin, Phys. Rev. C 70 (2005) 045804;
J.Serrau, C.Volpe, Phys. Rev. C 70 (2005) 055502.

		V	a	R	V_s	a_s	R_s	R_c
		[MeV]	[fm]	[fm]	[MeV]	[fm]	[fm]	[fm]
^{12}C	p	-55.00	0.50	2.95	-4.00	0.50	2.95	2.95
	n	-55.00	0.50	2.95	-5.50	0.50	2.95	-
^{16}O	p	-52.50	0.53	3.2	-7.00	0.53	3.20	3.20
	n	-52.50	0.53	3.2	-6.54	0.53	3.20	-

Table 1: Parameters of Wood-Saxon type potential, see Eqs. (1,2,3), for ^{12}C and ^{16}O . The label p refers to protons and n to neutrons.

		^{12}C		^{16}O	
		WS	exp	WS	exp
p	1s1/2	-30.90		-29.90	
	1p3/2	-15.76	-15.96	-16.92	-18.44
	1p1/2	-12.95	-1.94	-12.74	-12.11
	1d5/2	2.0		-3.76	-0.60
	2s1/2			-0.89	-0.10
n	1s1/2	-34.04		-33.98	
	1p3/2	-18.92	-18.72	-20.52	-21.81
	1p1/2	-15.06	-4.96	-16.63	-15.65
	1d5/2	-3.88	-1.10	-6.84	-4.14
	2s1/2	-1.96	-1.86	-3.90	-3.27
	1d3/2	1.6		-3.90	-3.27

Table 2: Single particle energies in MeV for protons (p) and neutrons (n) states. The label WS indicates the theoretical results. The experimental energies have been deduced from the level schemes of the neighboring nuclei [21]. The horizontal lines indicate the Fermi surface. This is the discrete part of the configuration space used in the CRPA calculations.

	F^{ext}	F^{int}	F'^{ext}	F'^{int}	G	G'	$\mathcal{K} (^{12}\text{C})$	$\mathcal{K} (^{16}\text{O})$
LM1	-740.0	60.4	453.0	453.0	166.1	211.4	0.8	0.865
LM2	-630.0	0.0	450.0	195.0	0.0	300.0	1.0	0.865
PP	-1007.0	-54.7	677.8	201.3	60.0	241.0	1.2	1.030

Table 3: Values of the parameters, in MeV fm^3 , of the three forces used in our calculations, see Eq. (4). The \mathcal{K} factors renormalize the forces.

	$^{12}\text{C} \rightarrow ^{12}\text{C}$	$^{12}\text{C} \rightarrow ^{12}\text{B}$	$^{12}\text{C} \rightarrow ^{12}\text{N}$
LM1	13.80	11.28	17.08
LM2	13.89	11.36	17.19
PP	12.94	11.23	17.03
exp	15.11	13.37	17.34

Table 4: Excitation energies, in MeV, of the 1^+ states in ^{12}C for charge-conserving excitation and charge-exchange excitations. Experimental energies are from Ref. [21].

ε [MeV]	A [MeV]	B [MeV]	C [MeV]	m^*/m
10.0	6.0	60.0	110.0	1.0
40.0	11.0	20.0	110.0	0.85

Table 5: Parameters of the function $\gamma(\varepsilon)$, Eq. (12), and of the nucleon effective mass. The values of the upper row have been used for $\varepsilon \leq 10$ MeV. Those of the lowest row for $\varepsilon \geq 40$ MeV. For intermediate energies we used values obtained by making a linear interpolation between those given in the table.

J^Π	(e, e')	(ν, ν')	$(\bar{\nu}, \bar{\nu}')$	(ν, e^-)	$(\bar{\nu}, e^+)$
$\theta = 30^\circ$					
1^-	0.93	0.47	0.49	0.30	0.28
1^+	< 0.01	0.04	0.04	0.03	<0.01
2^-	< 0.01	0.43	0.39	0.57	0.69
2^+	0.05	0.02	0.04	<0.01	<0.01
<i>oth</i>	0.02	0.04	0.04	0.10	0.03
$\theta = 150^\circ$					
1^-	0.63	0.48	0.50	0.49	0.28
1^+	0.01	0.04	0.04	0.03	0.02
2^-	0.15	0.43	0.39	0.45	0.63
2^+	0.18	0.02	0.04	0.01	0.03
<i>oth</i>	0.03	0.03	0.03	0.02	0.04

Table 6: Percentage contribution of the various multipoles to the energy integrated cross sections of Fig. 7. The rows labeled *oth* give the contribution of the multipoles other than those labeled in the Table up to $J=12$.

	RPA	FSI
LM1	5.17	4.48
LM2	8.12	7.15
PP	7.70	5.77
	14.1±1.6±1.9	[47]
exp	14.8±0.7±1.4	[48]
	14.0±1.2	[49]

Table 7: Total $^{12}\text{C}(\nu, e^-)^{12}\text{N}$ flux averaged cross sections, in 10^{-16} fm^2 units, for electron neutrinos emitted from muon decay at rest.

	T [MeV]	α	$\langle \varepsilon_i \rangle$ [MeV]
I	3.49	0.0	11.0
II	3.80	0.0	12.0
III	2.46	4.0	11.0

Table 8: Parameters used in the energy distribution $f(\varepsilon_i)$, Eq. (17), and the respective average energies.

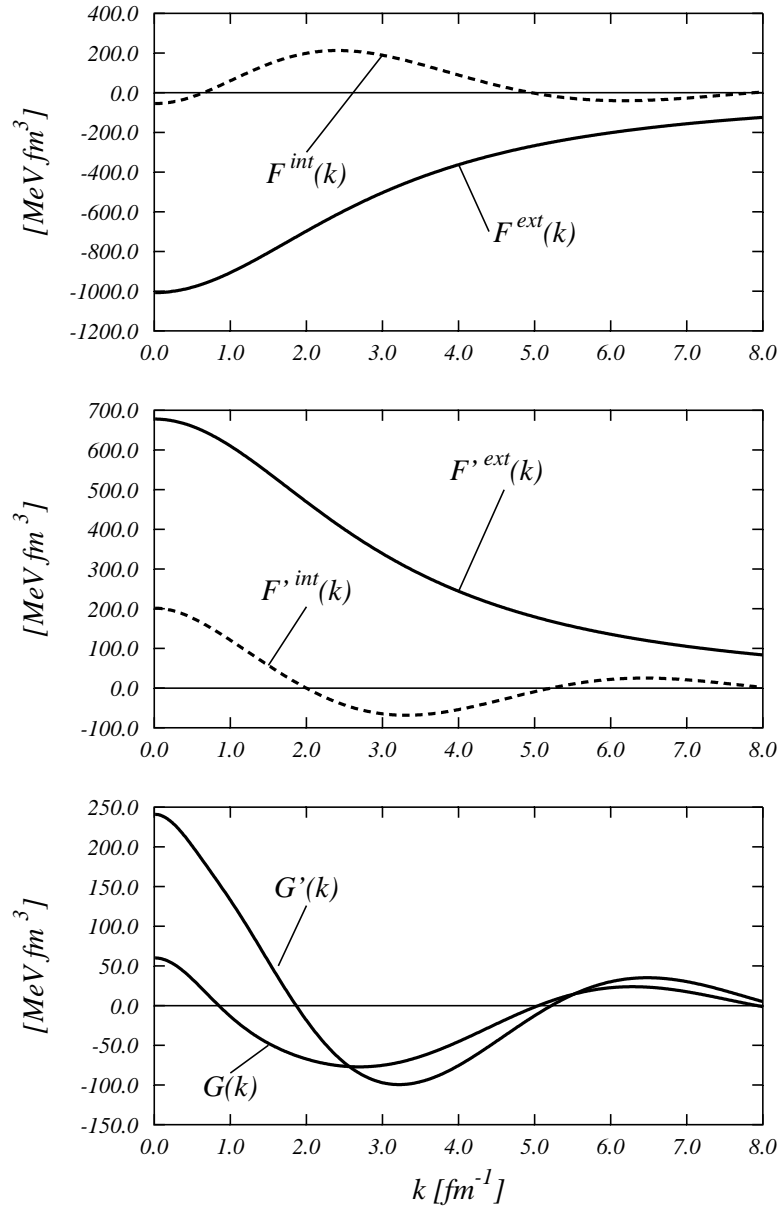


Figure 1: The various terms of the PP interaction as a function of the nucleons pair relative momentum k .

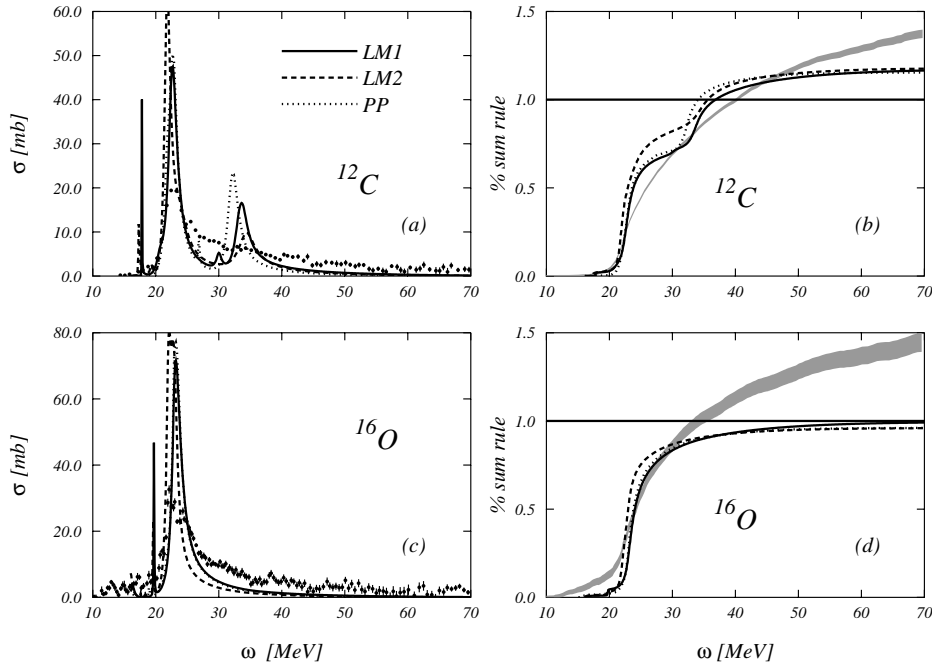


Figure 2: Panels (a) and (c): total photo-absorption cross sections of ^{12}C and ^{16}O calculated with the CRPA, compared to the experimental data of Ref. [10]. In the panels (b) and (d) we show the sum rules calculated as integral of the cross sections shown in panels (a) and (c), see Eq. (7), and normalized to the classical value of the Thomas-Reiche-Kuhn sum rule. The gray bands indicate the experimental sum rules. The LM1, LM2, and PP labels refer to the three different residual interactions used in our work.

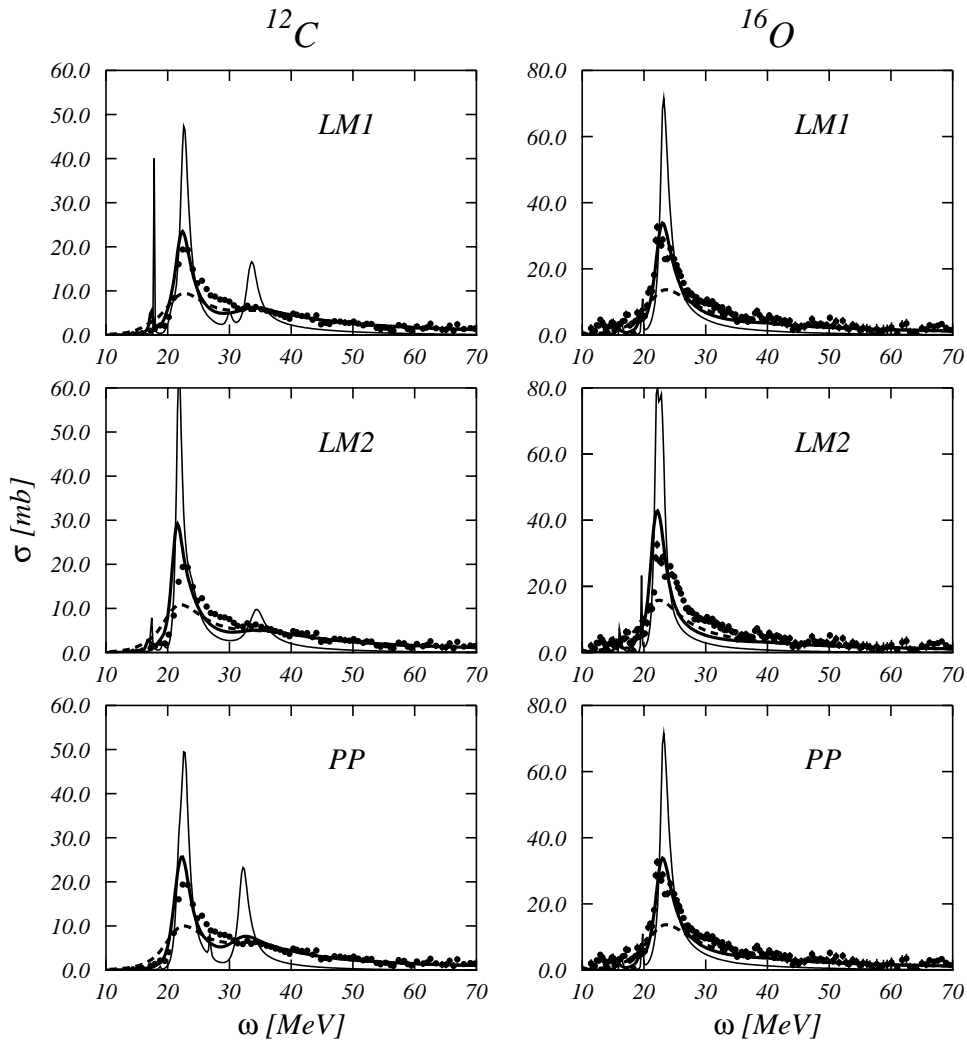


Figure 3: The full thin lines show the CRPA results, while the full thick lines have been obtained by applying our energy dependent FSI model. The data are from Ref. [10] and the labels of each panel indicate the residual interaction used in the calculation. The dashed lines show the results when the parameters given in lowest row of Table 5 are used.

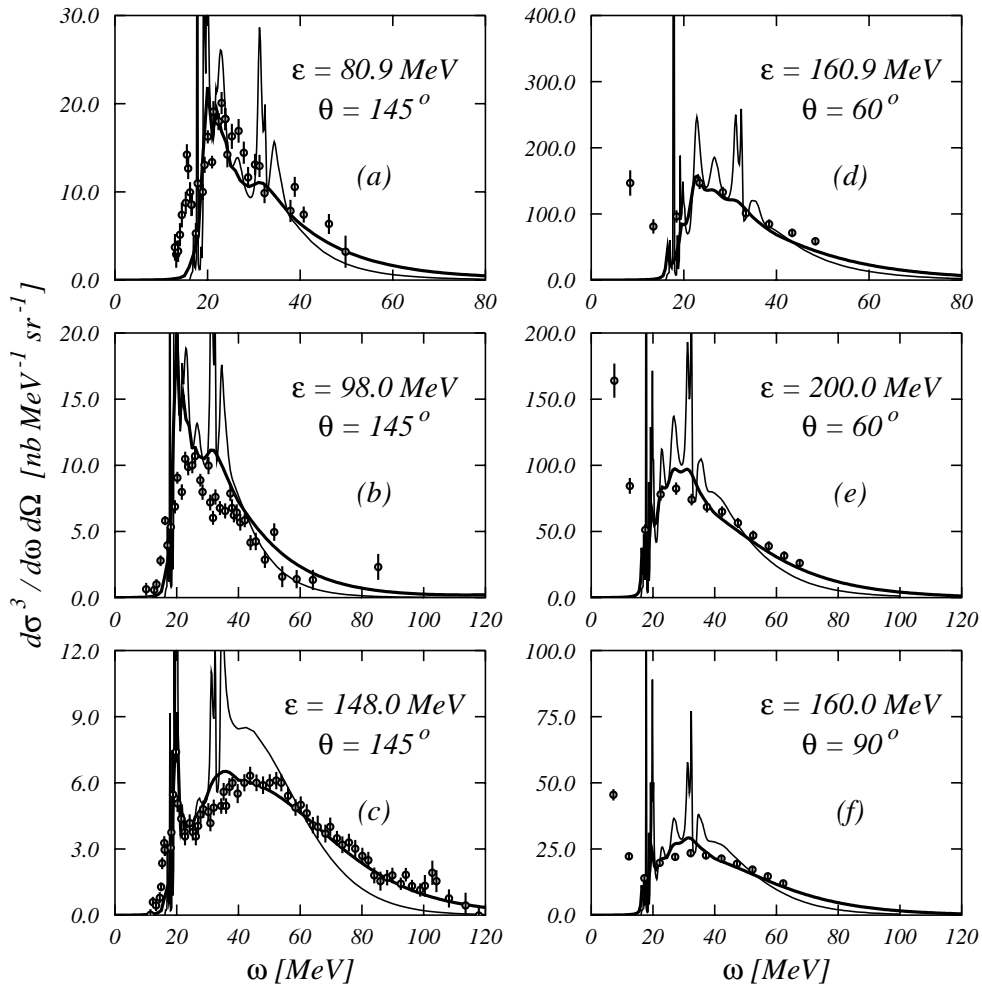
$^{12}\text{C}(e,e')^{12}\text{C}$


Figure 4: The thin lines show the CRPA results, while the thicker lines have been obtained by applying the FSI folding model. The LM1 interaction has been used in all the calculations. The data shown in the (a), (b) and (c) panels are those quoted in Ref. [35], while the data of the other three panels have been measured in Saclay [34].

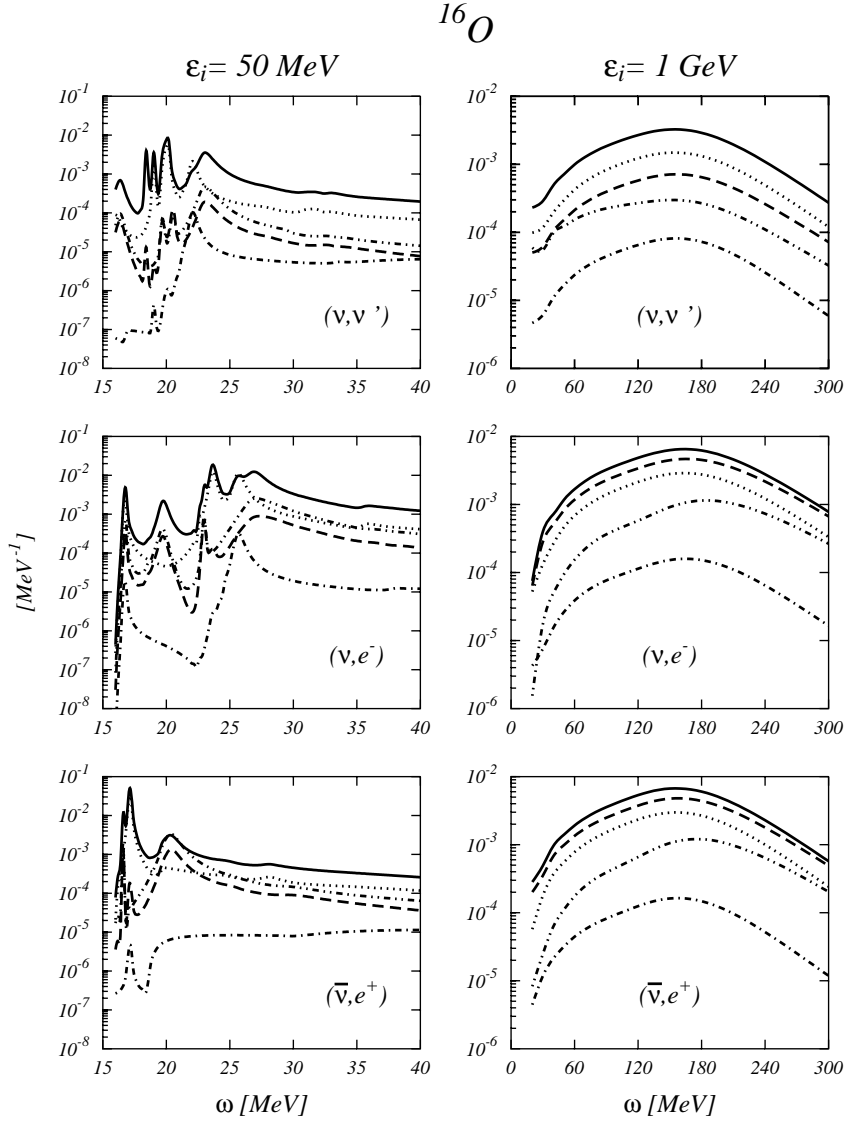


Figure 5: Weak responses calculated for $\theta = 30^\circ$ and for two different values of the lepton energies. The full lines show the transverse axial vector responses. See the text, section 3.1, for the meaning of the other lines.

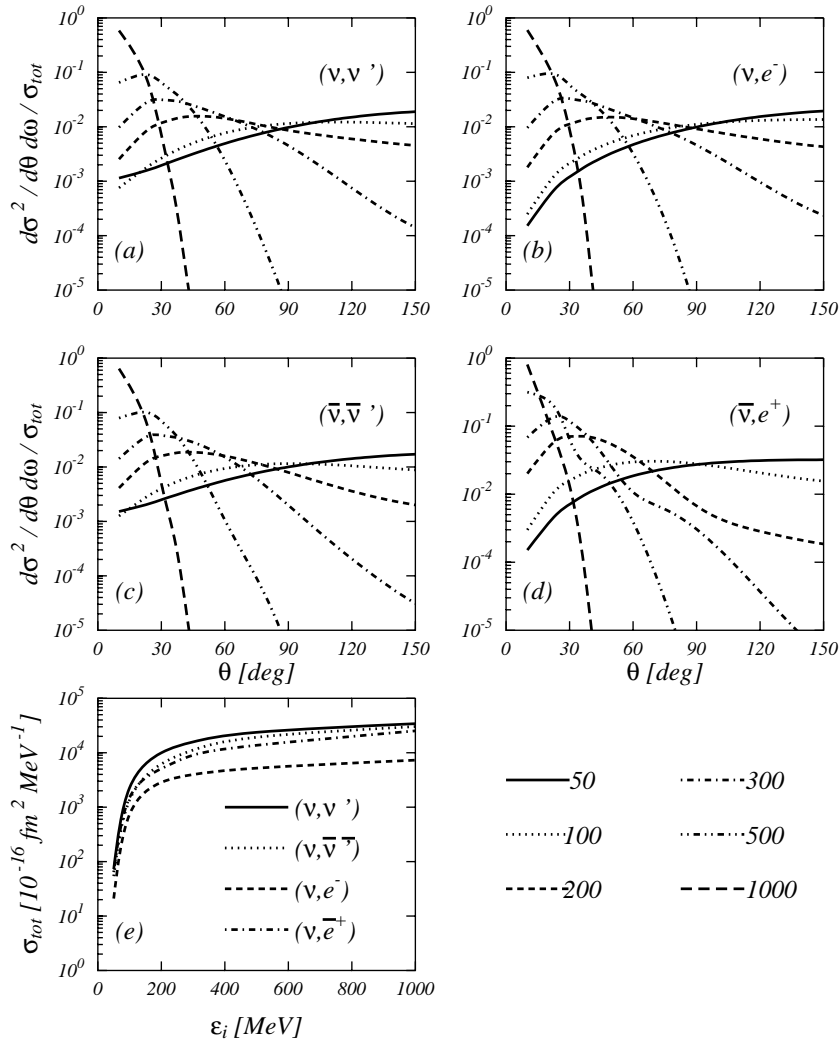


Figure 6: The (a) – (d) panels show the ratios between the doubly differential cross sections and the angular integrated cross sections σ_{tot} as a function of the scattering angle θ . The target nucleus is ^{16}O . The excitation energy for all the calculations is 20 MeV. The various lines have been obtained by changing ε_i , the projectile energy, whose values in MeV are indicated in the lower part of the figure. In the panel (e) we show σ_{tot} as a function of ε_i .

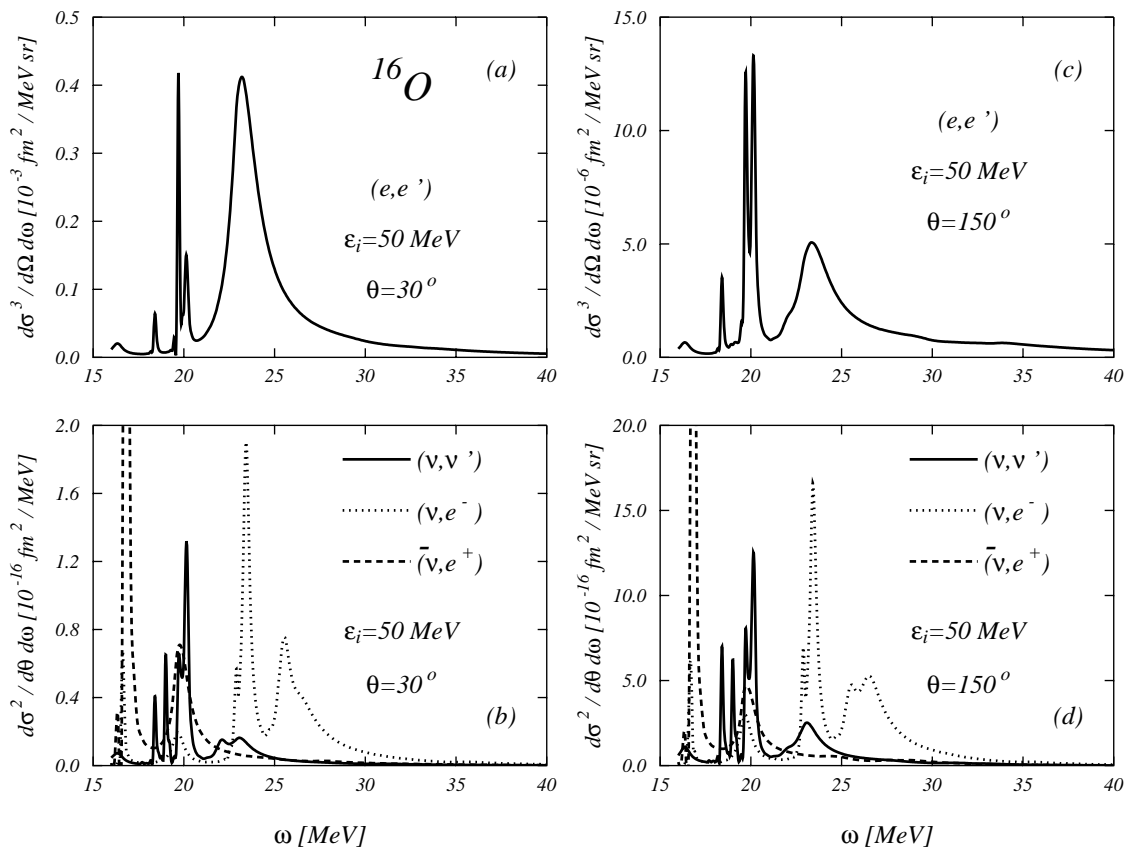


Figure 7: Double differential cross sections for electron and neutrino scattering processes, as a function of the nuclear excitation energy ω . The calculations have been done in CRPA with the LM1 interaction. Multipoles up to $J=12$ have been considered. In each panel, the incoming energy ε_i and the scattering angle θ , are specified. The 10^{-16} fm^2 units correspond to the more commonly used 10^{-42} cm^2 units.

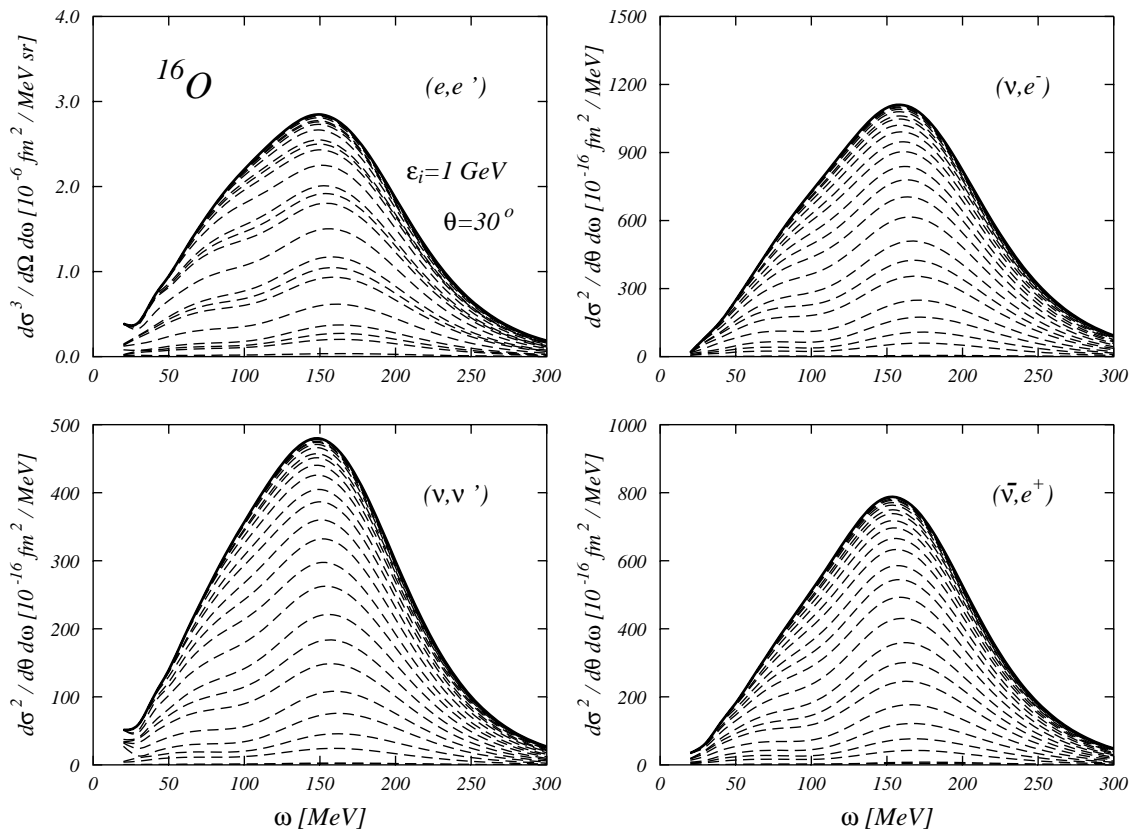


Figure 8: The same as in Fig. 7 in the quasi-elastic region. The thin broken lines indicate the contribution of each multipole excitation to the total cross sections represented by the thick full lines. These contributions are summed one on top to the other ones, and they are ordered with increasing value of angular momentum J . For a value of J , we give first the contribution of the negative parity state, and after that of positive parity.

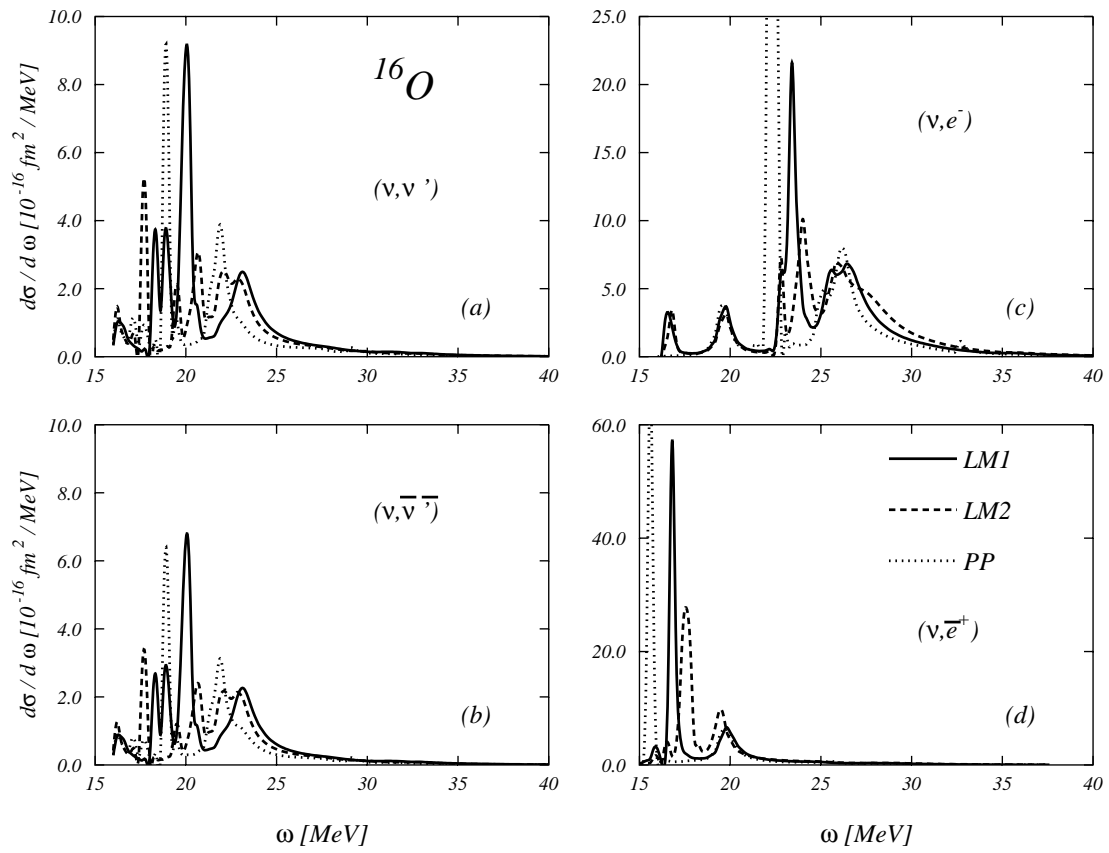


Figure 9: Differential cross sections on the ^{16}O nucleus for various neutrino reactions integrated on the angular distributions, as a function of the nuclear excitation energies. In all the cases the values of the projectile energy, ε_i , is 50 MeV. The various cross sections have been calculated with the CRPA by using the three interactions adopted in this paper. The meaning of the lines is given in the panel (d).

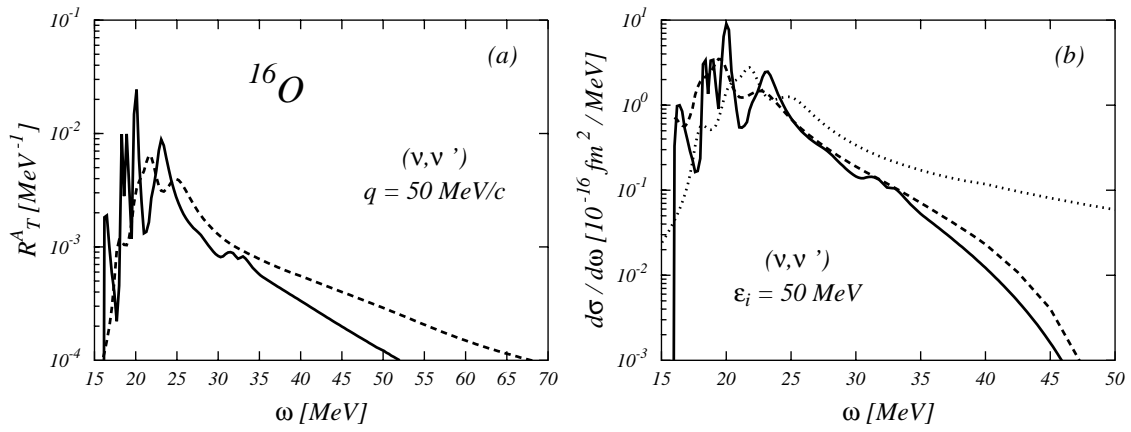


Figure 10: In panel (a) the ^{16}O transverse axial response at $q = 50 \text{ MeV}/c$ for the (ν, ν') process is shown as a function of the nuclear excitation energy. The full line show the CRPA result obtained with the LM1 interaction, the dashed line show the result of the folding procedure. In panel (b) the angular integrated cross sections for the (ν, ν') process are shown as a function of the excitation energy. The full line shows the CRPA result. The dotted line is the result obtained when the folding procedure is applied to the cross section. The dashed line has been obtained by applying the folding procedure to the responses.

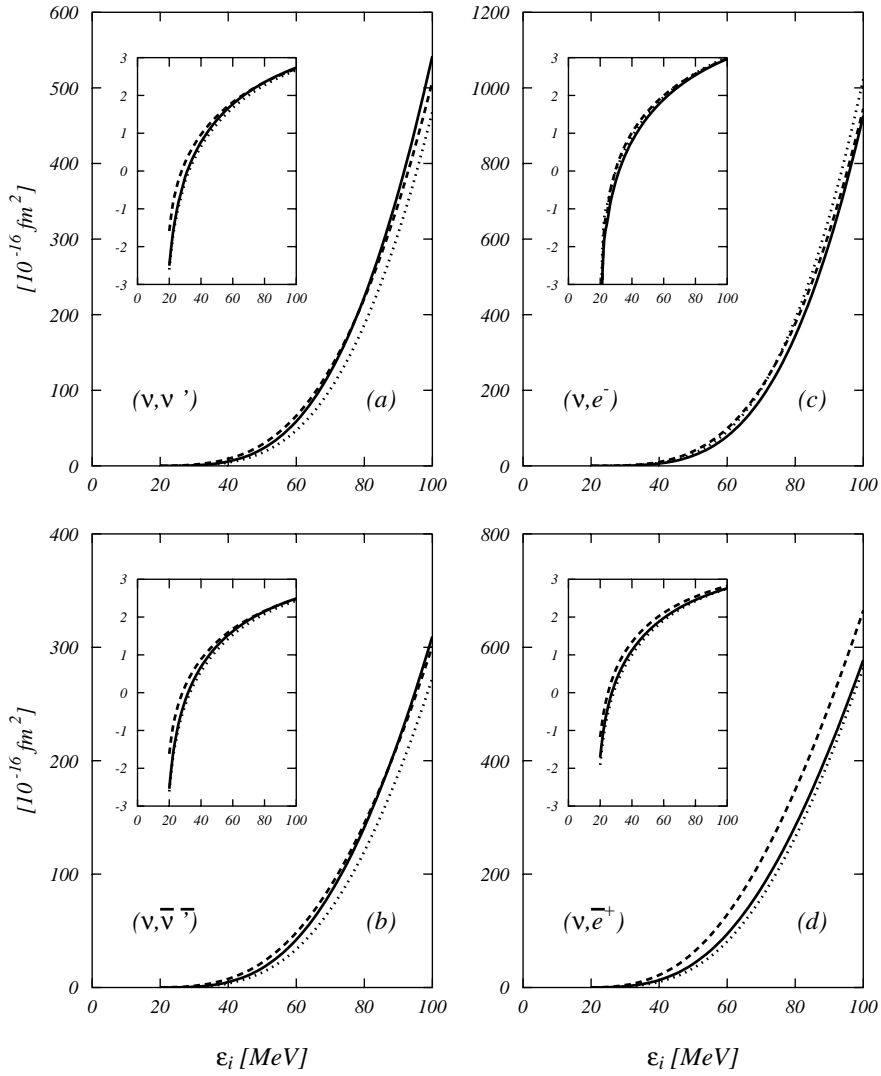
^{12}C 

Figure 11: Total cross sections on a ^{12}C target as a function of the projectile energy ε_i . The full lines show the LM1 results, the dashed lines the LM2 results and the dotted lines the PP results. In the inserts, the same curves are shown in logarithmic scale. The numbers on the y axes indicates the powers 10 of the logarithm.

^{16}O

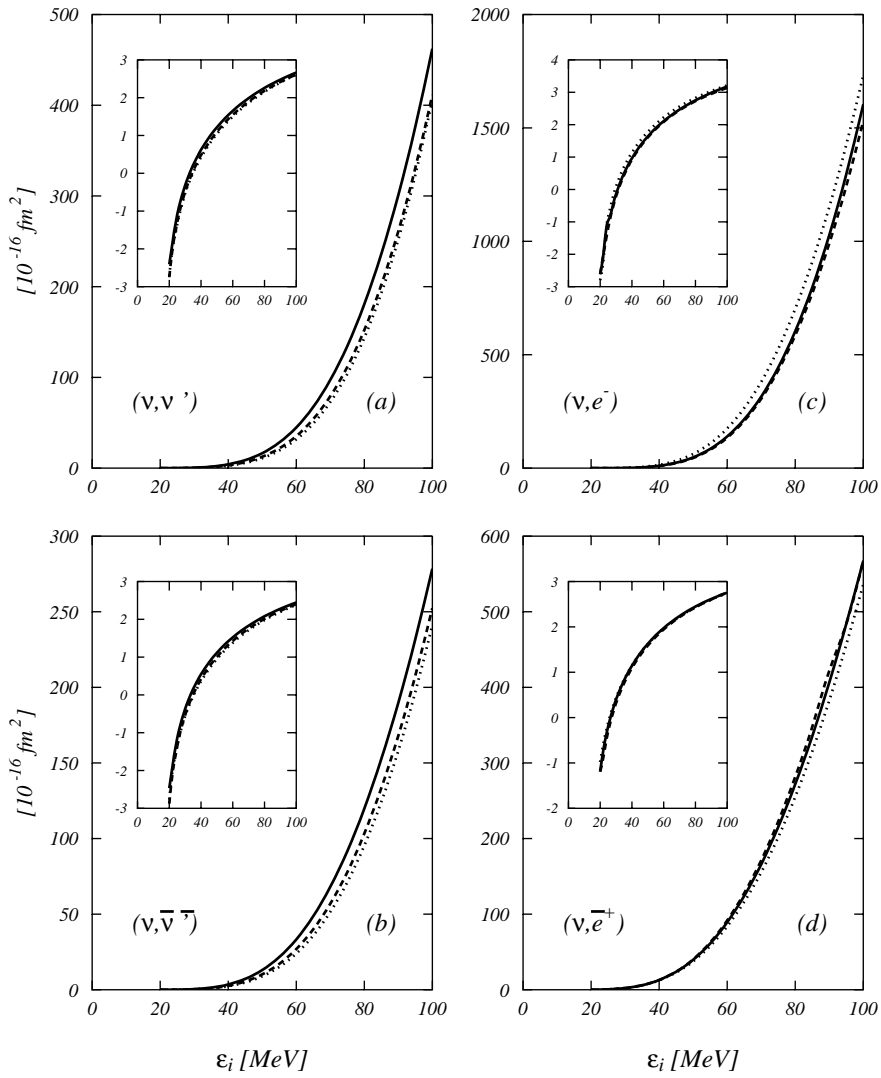


Figure 12: The same as Fig. 11 for the ^{16}O nucleus.

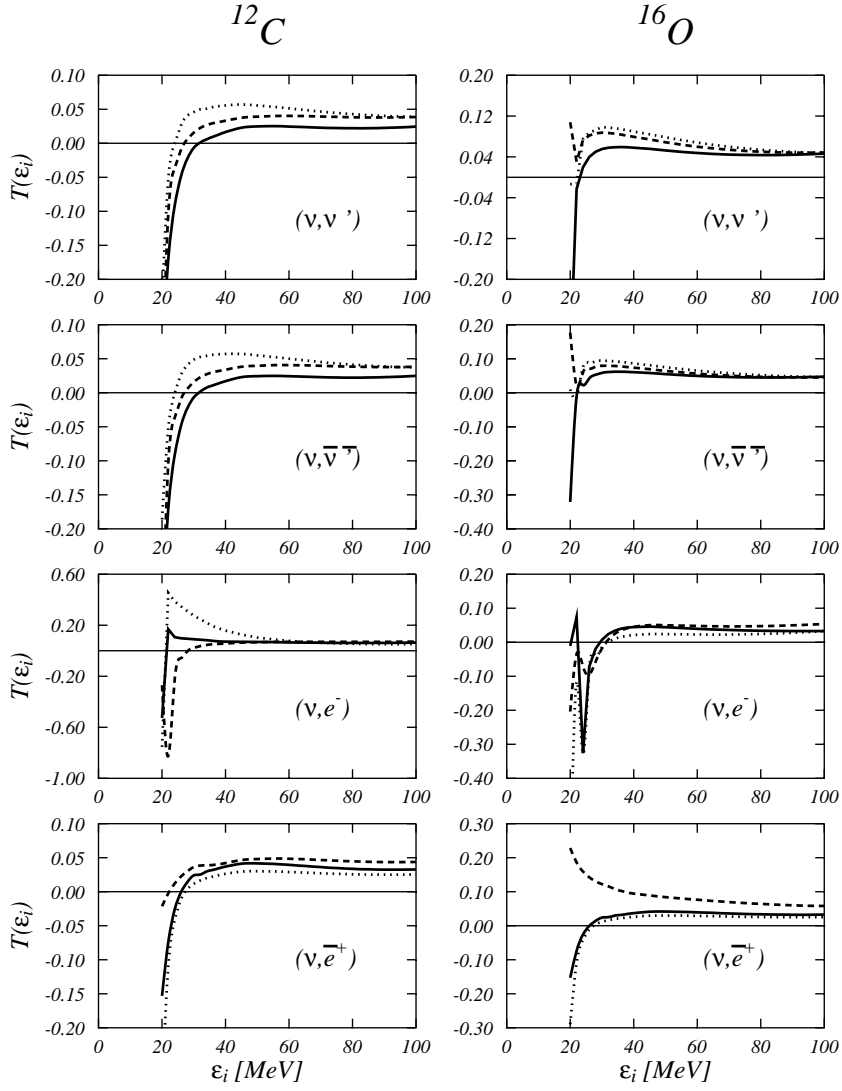


Figure 13: Ratio $T(\varepsilon_i)$, Eq. (14), for the four neutrino interactions considered in this work. As in the previous figures, the full lines show the LM1 results, the dashed lines the LM2 results and the dotted lines the PP results.

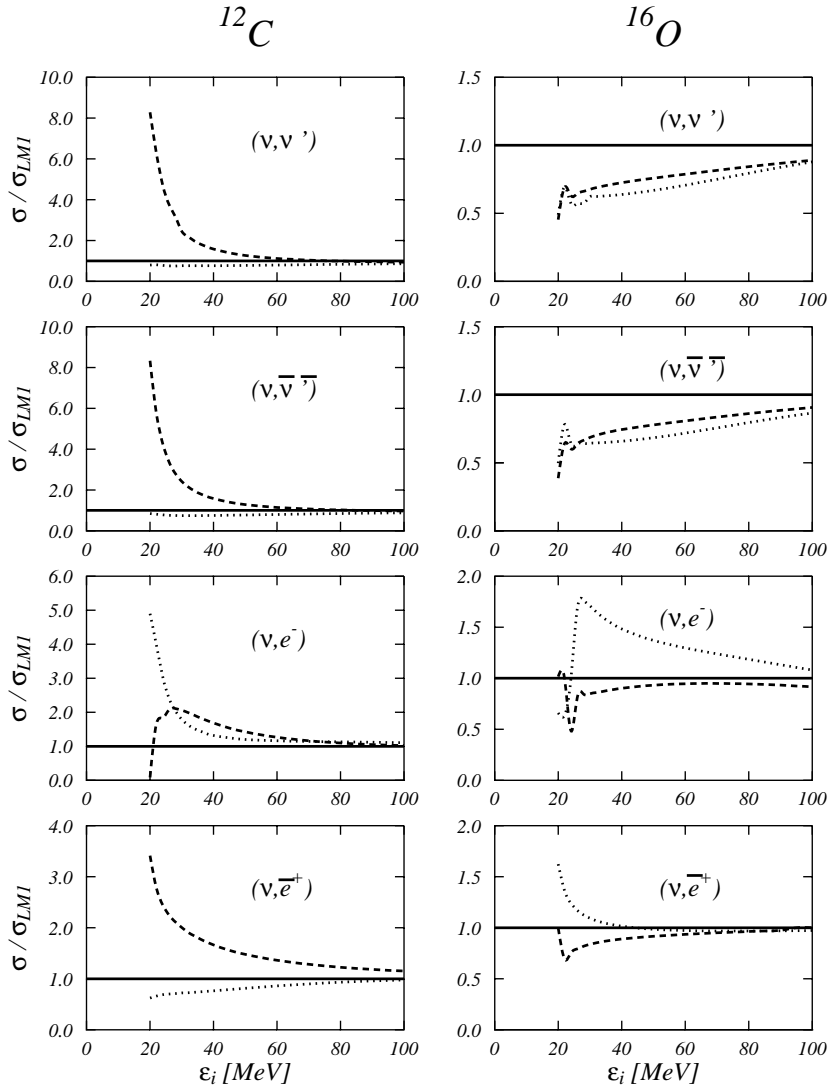


Figure 14: Ratios between the total cross sections of Figs. 11 and 12 and the LM1 cross sections. The dotted and dashed lines show the PP and LM2 ratios, the full horizontal line with value 1, refers to the LM1 results.

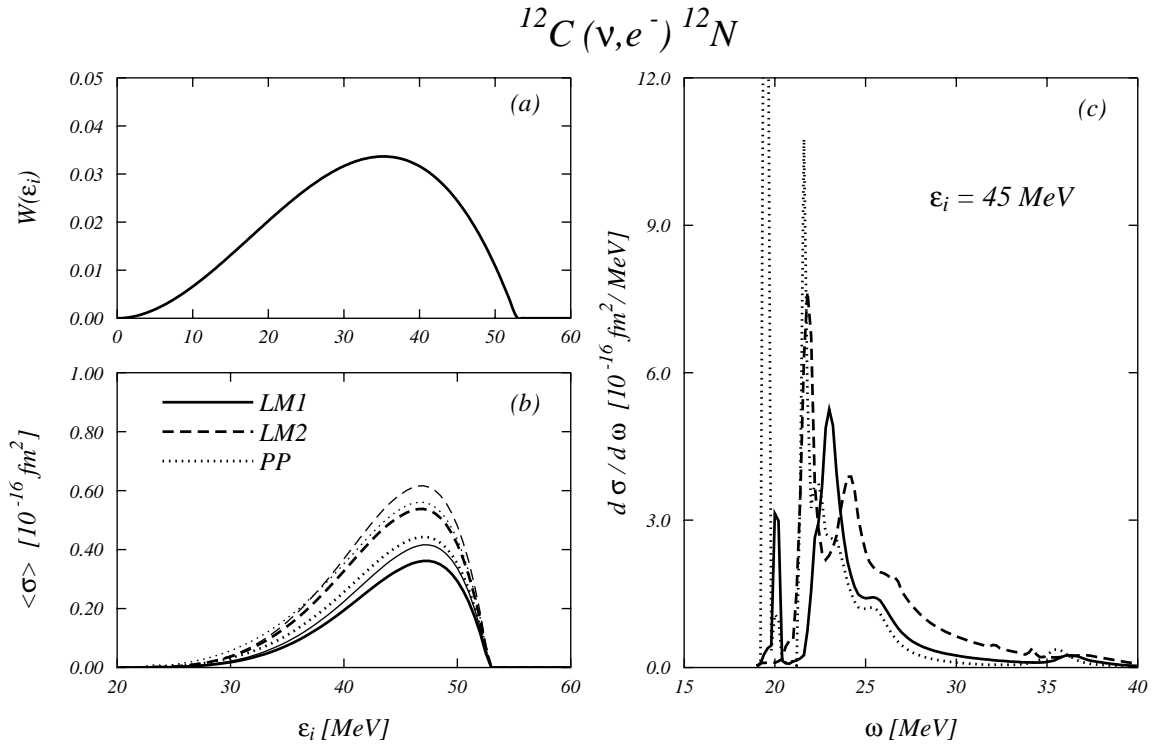


Figure 15: In panel (a) we show the normalized neutrino flux coming from the neutrino decay at rest. In panel (b) the flux averaged cross sections are shown as a function of the neutrino energy. The thin lines have been obtained by folding the CRPA results and the thicker lines with the FSI included. The different line types indicate the residual interactions used in the calculations. The CRPA differential cross sections for $\epsilon_i = 45$ MeV are shown in panel (c) as a function of the nuclear excitation energy.

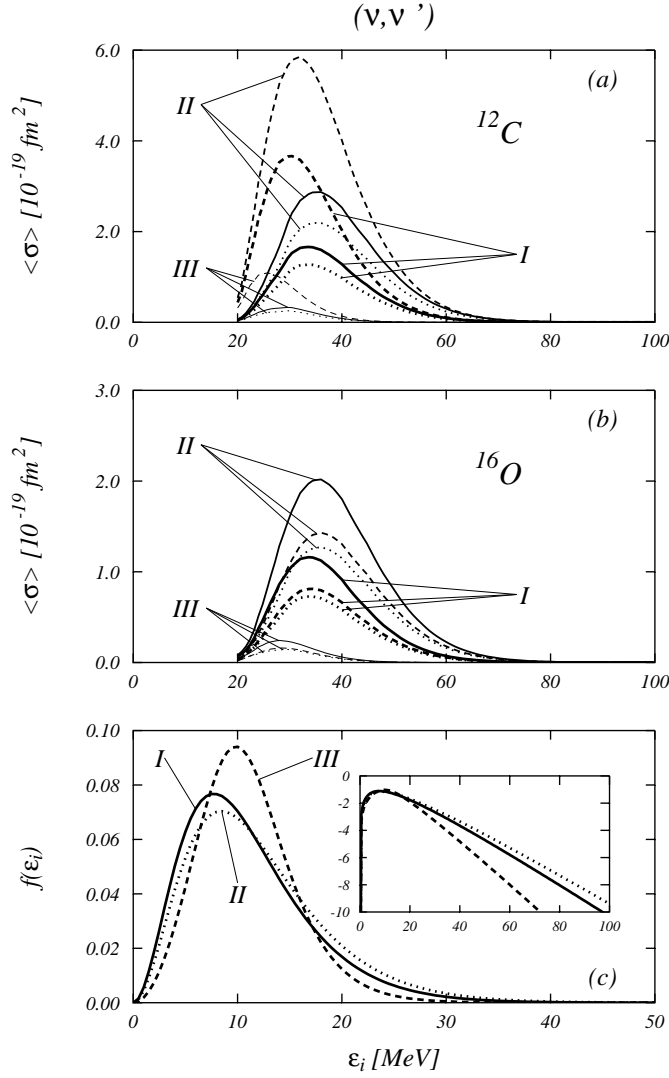


Figure 16: Total (ν, ν') cross sections averaged with the energy distribution (17). The roman numbers refer to the parameters of $f(\varepsilon_i)$ given in Table 8. In the panels (a) and (b) the different line types refer to the residual interactions used in the calculations. As in the previous figures, the full lines indicate the results obtained with LM1, the dashed lines those obtained with LM2 and the dotted lines the results obtained with the PP. The three energy distributions $f(\varepsilon_i)$ are shown in the panel (c). In the insert the same lines are shown in semi-log scale.